2

SYNTHESIS OF OPTIMUM MICROWAVE ANTENNA APPLICATORS FOR USE IN TREATING DEEP LOCALIZED TUMORS

Carey M. Rappaport

2.1 Electromagnetic Power Deposition in Lossy Media and Hyperthermia

a. Introduction

Electromagnetic interaction with matter, though less widely studied than radiowave communication and guidance, has many important technological applications. Waves penetrate through media in well-understood ways, with sensitive phase and amplitude information changing depending on the size, shape, and electrical characteristics of obstacles encountered. Electromagnetic waves find use in nondestructive evaluation, remote sensing, tomographic imaging, and medical evaluation and treatment. Higher power electromagnetic fields are also useful for sealing in the plastics industry, for bulk drying and sterilizing, and for controlled medical heating. Radio-frequency diathermy devices are used for deep heating of injured or afflicted muscles. Perhaps the most challenging but beneficial use of medical heating is hyperthermia cancer treatment [1]. The optimized delivery of power below the surface of idealized lossy structures is examined in this chapter. Specifically addressed is the problem of determining the limitations and best strategies for non-invasively heating tumors without harming the surrounding healthy tissue.

Cancer is the second greatest cause of death in the developed world. About one out of every four persons will eventually contract the disease. Cancer takes many forms, from solid tumors in organs, bone, and muscle; to systemic neoplasias of blood and lymph; to superficial lesions such as melanoma of the skin. Survival rates vary greatly, depending on type of cancer and time of detection.

Currently, there are three primary means of treating cancer: surgery, radiation, and chemotherapy. Of the approximately 700,000 diagnosed life-threatening cases of the disease in 1977, 190,000 did not respond to any of these treatments and an additional 155,000 patients had a high risk of cancer recurrence [2].

Cancer surgery is the major means of treating localized, solid tumors. For surgical treatment of primary cancer, a macroscopic, recognizable tumor is resected along with a margin of surrounding tissue [3]. However, it has been estimated that about 70% of solid tumors will have micrometastases, or extensions into normal tissue [2], which often lead to recurrences of the disease.

Radiation therapy makes use of two main types of ionizing radi-

ation: electromagnetic, including X-rays and γ-rays; and particle radiation including beta, alpha, neutron, proton, and negative π-meson [4,5]. Therapy can take the form of either bachytherapy, where a radioactive device is implanted in or near a tumor, or teletherapy, where a beam is externally aimed toward the tumor.

Radiation has its greatest effects on cells which are most rapidly reproducing. Normal tissues which reproduce to function, such as the skin, bone marrow, gastrointestinal mucosa, and reproductive organs, are most sensitive to radiation. Radiation damage to these tissues must be carefully considered prior to treatment.

Chemotherapy treats the systemic spread of the cancer using toxic drugs which harm both neoplastic and normal cells, with the hope that the former are more sensitive. Most of the chemotherapeutic drugs are primarily effective in killing dividing cancer cells as opposed to resting cells. Unfortunately, as tumors grow, a greater percentage of cancerous cells convert from actively dividing to a resting state, and thus avoid the cytotoxicity of the drugs. Methods to accelerate the onset of the dividing cycle improve the performance of chemotherapy.

The use of heat to treat cancer is a relatively new modality, still in its experimental stages despite knowledge of its benefits as early as Roman times [6]. The first published account of hyperthermia was in 1866: W. Busch reported the selective effect of heat on tumors over normal tissue with the cure of facial sarcomas following a high fever caused by a streptococcal skin infection [7].

Starting in 1971, several studies established therapeutic temperature data [8–10]. The minimum temperature for therapeutic benefit is most often cited to be 41.8° C [7]. Although this relatively low temperature kills tumor cells slowly, it may have a preferential effect on malignant cells, leaving normal cells unaffected [11].

In living humans, tumors tend to overheat more easily than normal surrounding tissue "because their neovascularity is physiologically unresponsive and cannot augment blood flow to adapt to thermal stress" [12]. Whereas the blood flow in a tumor will not change noticeably when heated to 43° C, it will increase 160–360% in the surrounding tissue [13,14]. And since the cooling effect due to blood perfusion is usually 4 times that of conduction to neighboring tissue (and may be as high as 100 times in certain structures, such as kidney), a large difference in perfusion rate would prevent a tumor from cooling as much as healthy tissue.

Hyperthermia is effective in conjunction with other conventional modalities of cancer treatment, particularly ionizing radiation [16–18]. There is an additive, or synergistic effect between heat and X-rays [18]. It takes two-thirds the radiation dose to achieve the same fraction of cell survival when hyperthermia is also used [6]. Heat tends to overcome radioresistance of some tumors, and may prevent the repair of sub-lethal damage or cause mis-repair of DNA [13,19]. Hyperthermia also appears to sensitize tumors to chemotherapeutic agents. Heating tissue by 4° C to the level of 41° C increases the tumor cell killing effect of the drug BCNU by 10,000 times [2].

b. Non-Invasive Generation of Hyperthermia

In most cases, it is preferable to generate heat within tissue without physically penetrating the body surface. Complicating effects such as anesthetizing, sterilizing, cutting, implanting a device, and then suturing the ill patient are serious drawbacks to surgical implantation. Also, a non-invasive applicator can be designed to surround the body part containing the tumor, taking advantage of constructive interference and focussing to concentrate more heat at the tumor than in the surrounding normal tissue.

The two broad classes of hyperthermia applicators are electromagnetic and ultrasound. Electromagnetic applicators radiate waves which propagate at the speed of light, 3×10^8 m/sec in vacuum, or slower in matter, and are characterized by both a propagation direction and a vector polarization. Ultrasound makes use of acoustic waves which cannot propagate in a vacuum and has a much slower velocity (about 1500 m/sec in soft biological tissue), and since it is a compressional wave, does not have a polarization attribute.

The entire spatial behavior of either type of wave is governed by the attenuation rate, α, and the propagation constant, β. A convenient representation in terms of the complex wave number is

$$k = \beta - j\alpha \tag{1}$$

where $j = \sqrt{-1}$. Any spatial features, such as peaks or troughs, will extend for a distance on the order of a wavelength. A major distinction between electromagnetic and ultrasound radiation is the much greater resolution and focussing ability of the latter. Since the propagation velocity of ultrasound is 200,000 times slower than that of electromagnetic waves, the propagation constant β is much bigger for a given

attenuation constant α. Thus spatial resolution and focussing is much greater for ultrasound wave then for electromagnetic waves.

Ultrasound, while having a much higher power peak resolution, faces considerable impedance mismatch at soft tissue boundaries with air or bone [20]. Air is relatively impenetrable, while reflections from bones produce large standing wave effects. Thus, areas such as the lung, gastrointestinal tract, pelvis, rib cage, and head are difficult to treat with ultrasound.

The frequency range used for electromagnetic heating is much broader than for ultrasound. Six frequencies are reserved for industrial and medical uses: 13.56, 27.12, 40.68, 433, 915, and the standard used in microwave ovens 2450 MHz. Although it is clear that with increasing frequency, penetration decreases, attenuation and resolution increase, and the ability to focus increases, the relative changes are quite nonlinear.

Different tissue responds in different ways to electromagnetic stimulation. Wave behavior is governed by the conductivity σ and the dielectric constant ϵ' of the medium. These parameters are often joined in a single expression for the complex dielectric permittivity

$$\epsilon = \epsilon_0(\epsilon' - j\epsilon'')$$

where

$$\epsilon'' = \frac{\sigma}{\omega\epsilon_0}$$

$$\epsilon_0 = 8.85 \times 10^{-12}\text{F/m} \tag{2}$$

The values of ϵ' and σ are determined experimentally as a function of radian frequency ω. Tissue electrical parameters can be divided into two groups: high water content, including muscle, blood, and organs; and low water content, including fat and bone [21]. These two groups are generally referred to as the muscle or the fat tissue cases.

A plot of the most recently established values of ϵ' and σ [12], [22–28] is shown in Fig. 2.1.1. Dissipated power obeys the equation

$$P = \frac{\sigma}{2}|\overline{E}|^2 \tag{3}$$

where $\overline{E}$ is the electric field vector. Thus, tissue with higher conductivity, for the same electric field, dissipates proportionally greater power.

The electrical and thermal properties of biological tissue *in vivo* in the frequency range 27 – 2450 MHz have been successfully modeled

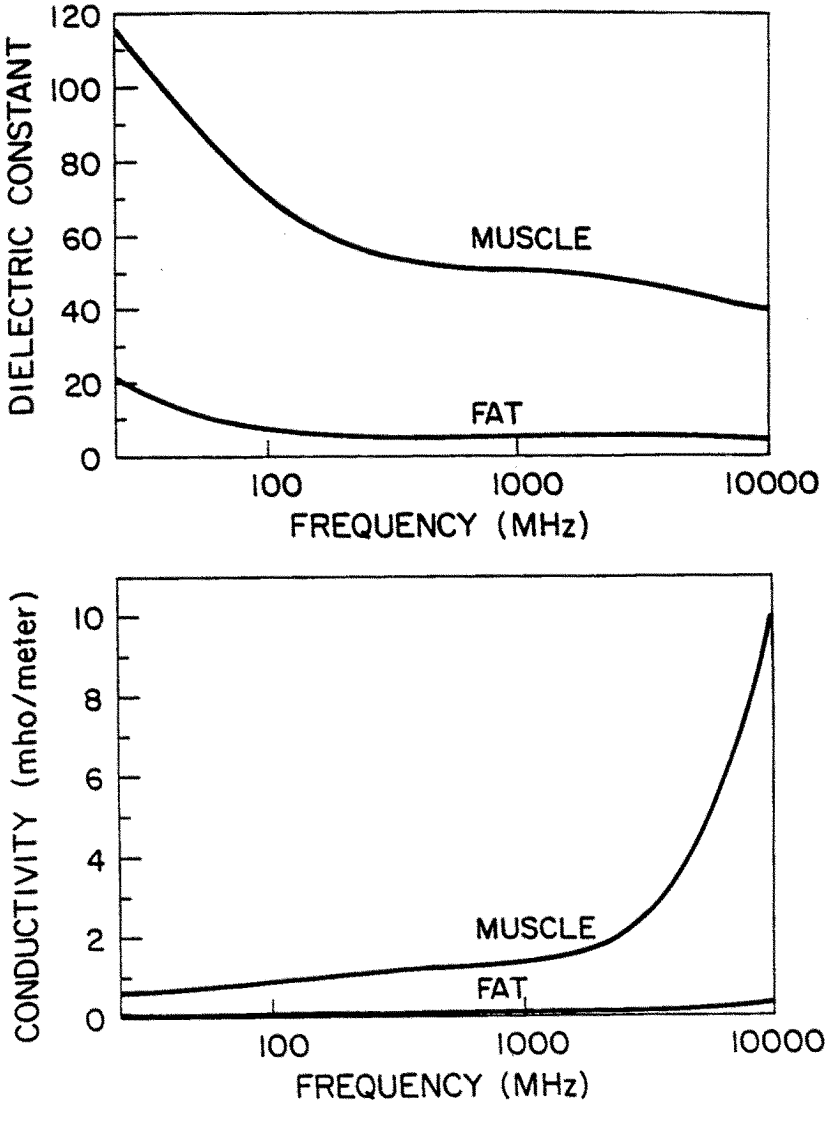

Figure 2.1.1 Electrical characteristics of high and low water content biological tissue as function of frequency (Data from Storm [12]).

with combinations of readily available substances. Guy [29] proposes a phantom recipe of 84.8% laminac polyester, 0.45% catalyst, 0.25% acetylene black, and 14.5% aluminum powder to simulate fat; and for a muscle phantom: 75.5% water, 0.9% salt, 15.2% polyethylene powder, and 8.4% TX–150 (a jelling agent). With slight proportion adjustments to compensate for different frequency variations, the resulting phantoms are very accurate dielectric models of living tissue.

From these values of the complex dielectric permittivity, the spatial parameters of the wave number of (1) can be determined. By definition, the dispersion relation for electromagnetic waves is

$$k = \omega\sqrt{\mu\epsilon} \tag{4}$$

where $\omega = 2\pi f$ is the radian frequency and μ is the magnetic permeability (taken in a biological tissue as the constant for free space, $4\pi \times 10^{-7}$ H/m). From (1) and (2), using the speed of light $c = 1/\sqrt{\mu_0\epsilon_0}$, and solving for the real and imaginary parts of the square of (4) yield

$$\beta = \frac{\omega}{c\sqrt{2}}\left[\sqrt{\epsilon'^2 + \left(\frac{\sigma}{\omega\epsilon_0}\right)^2} + \epsilon'\right]^{1/2}$$

$$\alpha = \frac{\omega}{c\sqrt{2}}\left[\sqrt{\epsilon'^2 + \left(\frac{\sigma}{\omega\epsilon_0}\right)^2} - \epsilon'\right]^{1/2} \tag{5}$$

Since $\lambda = 2\pi/\beta$, it is now possible to determine the muscle tissue wavelength for the frequencies of interest. Table 2.1.1 [30] lists the tissue wavelengths as well as the ratio α/β, which determines the amount of decay in each cycle. Also listed in the last two columns are maximum dimensions for heating idealized muscle volumes, which will be referred to in sections 2.3 and 2.4.

An important point is the matching of impedances from the applicator to tissue. Unless the waveguide is loaded with dielectric with the same complex permittivity as the tissue being heated, there will be an electrical impedance mismatch. The mismatch causes reflection which prevents the complete transfer of power into tissue and contributes strongly to stray radiation. The mismatch may be reduced by

inserting a matching layer composed of lossless dielectric of intermediate constant with specific thickness between the applicator and the tissue. If the tissue were lossless, the ideal layer would be a one-quarter wavelength thick section of material with dielectric constant equal to the geometric mean of that of the tissue and applicator material. With actual lossy tissue, the thickness and dielectric constants are slightly different.

Table 2.1.1 Attenuation to propagation ratio, tissue wavelength, and maximum penetration slab thickness and diameter, as a function of frequency, for muscle tissue.

f (MHz)	α/β	WAVELENGTH IN TISSUE (cm)	SLAB THICKNESS	MAX D
27	.76	68	20.6	36
41	.73	51	16.2	29
100	.65	27	11.2	19
433	.40	8.8	5.6	11.5
750	.27	5.3	3.8	11.8
915	.23	4.5	3.4	12.6
1500	.20	2.8	2.2	9.6
2450	.17	1.8	1.5	7.7

This matching layer is often incorporated into a bolus. A bolus filled with a circulating liquid or high thermal conductivity powder would conform to irregular body contours and provide skin surface cooling.

The advantages and disadvantages of the various non-invasive methods of generating hyperthermia are summarized in Table 2.1.2 [21,13].

Table 2.1.2 Comparison of methods of using waves to generate hyperthermia.

Ultrasound

Advantages

Simple to use, fat not preferentially heated, does not interfere with temperature measurements, tumors absorb ultrasound better than normal tissue; no significant reflection from muscle/fat boundaries; precise localization possible; focussing depth as great as 15 cm

Disadvantages

Differential heating of bone; Coupling to uneven surface difficult; air/tissue interface causes reflections; inability to heat lung, abdomen; volume to be heated limited by size and number of transducers or scanning time

Electromagnetic, Capacitive

Advantages

Can design applicator for specific patient needs; can heat large volumes; skin easily cooled

Disadvantages

Skin and fat preferentially absorb power and heat; heating pattern hard to predict; metal temperature probe perturbs field, gives false readings

Electromagnetic, Inductive

Advantages

Simple coils; preferential heating of muscle; can heat large volumes; direct contact unnecessary.

Disadvantages

Weak tissue coupling, non-uniform field; heat not easily localized; metal temperature probes are corrupted

Electromagnetic Microwave

Advantages

Muscle tissue preferentially heated; can heat in presence of air, i.e., lung, stomach, bowel, rectum, pelvis; can heat near bones, brain; penetrates well in fat, high resolution focus; localization can be readily directed

Disadvantages

Limited penetration depth; shielded room may be needed to contain hazardous leakage radiation, focussing not useful for low frequencies; metal temperature probes are corrupted; potential danger to pacemakers; applicator may be awkward

c. Microwave Source Synthesis for Producing Constructive Interference at Depth

The goal of any hyperthermia source synthesis is simple to state: to generate a power pattern with more power in the vicinity of a focal target than anywhere else, and thus heat the tumor without overheating healthy tissue.

Attenuation rate varies directly (though nonlinearly) with frequency while field resolution decreases with increasing frequency. In human muscle tissue volumes, the "focus" is relatively wide and of low intensity. Generally, the sharpest focus — or highest resolution — corresponds to the highest possible frequency that deposits at least as much power at the tumor as at any point in the surrounding volume or on its surface. surface. Exceeding this frequency may produce higher resolution, but the actual safe maximum penetration depth into the tissue will be less.

More complicated than frequency selection is the determination of optimal source distribution. For constructive interference at a focus, electric field at the tissue surface must be properly aligned and phased so that waves propagating along all paths in the entire tissue volume arrive in the same fashion. While this simple condition is almost always met with planar applicators, cylindrical sources are often designed to produce a circumferential electric field, E_ϕ [31,32]. This choice of polarization is relatively easy to generate using a single turn, flat loop of conductor. Also, the circumferential polarization has the advantage of being transverse to tissue boundaries. However, if the aim is to produce power along the cylinder axis, the E_ϕ polarization is absolutely wrong. By intuitive reasoning, there can be no rotating field at the axis, $\rho = 0$, so E_ϕ, and hence dissipated power, vanishes at the axis.

Transverse polarization is preferable to normal (radial, in the case of a cylinder) polarization [33–35]. Capacitive electrodes, for example, are inefficient because the normal electric field heats subcutaneous fat. The normal electric field changes across a medium boundary in proportion to the ratio of the dielectric constants of the two media. Fat, with nine times less dielectric permittivity than muscle at 915 MHz, has 9 times the normal electric field. Transverse electric field, on the other hand, is continuous across media boundaries. According to (3), muscle tissue, with about 15 times the conductivity of fat, dissipates 15

times more power for the transverse polarization. But because of the squaring of electric field in (3), the normal polarization produces 81/15 as much power in the fat as in the muscle. Since tumors are usually found embedded in muscle tissue which in turn is surrounded by fat, it is much better to use tangential polarization which concentrates power on the muscle side of the muscle/fat boundary. The attenuation rate is much lower in fat than in muscle because of its lower conductivity. For typically thin subcutaneous fat layers, the power pattern is relatively constant. Furthermore, fat surrounds muscle, so keeping power at at reduced level in the fat reduces the overall problem to minimizing power maxima in a volume of muscle tissue.

Even though the thermal conductivity of fat tissue is relatively low, it still acts to cool a heated muscle tissue surface. Thus, for a first level analysis, as long as the electric field polarization is kept almost transverse to the muscle/fat boundary (and hence transverse to the skin), the fat layer can be ignored. Design considerations can thus be based on prescribing the source distribution on the muscle surface, assuming a constant temperature muscle surface boundary condition.

Merely adjusting phase, polarization, and amplitude for maximum focussing does not necessarily produce an acceptable power density distribution. Consider Fig. 2.1.2 with a planar source on the left, with phase adjusted to focus on the point labeled F, three tissue wavelengths into the lossy medium. That is, the phase at any source point is set to the negative of the physical distance from F to that point, times the tissue propagation constant β. This focussing is often referred to as a conjugate phase source distribution. Although F is the only point of coherence in the tissue, having significant gain over a uniform phase distribution as shown in Fig. 2.1.2b, the power there is still much lower than at points closer to the source, Fig. 2.1.2c, which experience less exponential wave decay. These plots were calculated for muscle tissue at 915 MHz, with electrical parameters taken from Storm [12], using 32-point Gauss-Legendre integration of the diffraction integral.

Several papers have dealt with this conjugate phase concept [36–39]. The frequencies used in their papers were all 433 MHz or above. The low electromagnetic frequencies would not be suitable for this focussing method because the source-to-focus path length variations

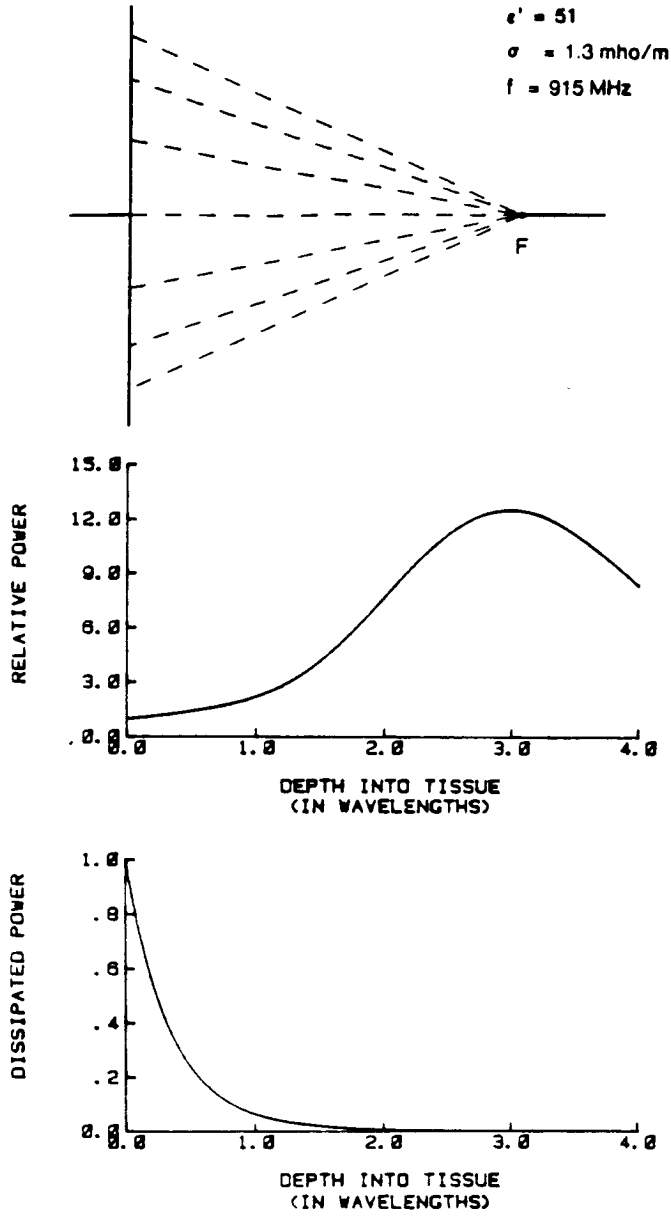

Figure 2.1.2 Focussing at depth: Fallacy of maximum intensity at focus in a lossy medium, (a) geometry, (b) relative power density, (c) power gain over uniform plane wave.

are less than a single tissue wavelength. Despite improvements of up to 9 dB at 2.7 wavelengths into muscle (6 cm) at 1500 MHz [39], the power is still 20dB below the power at the surface.

The conjugate method used by Gee et al., [37] is a useful proof-of-principle that irregular and inhomogeneous tissue samples can be illuminated with a focussed field almost as well as uniform tissue. The method involves measuring the field at the source points due to a test source placed at the focal point. The resulting phase represents the effective electrical path length through the irregular tissue volume. Unfortunately, it is difficult to place a test source in a tumor without facing the risks of invasive treatment outlined previously. Also, the method neglects the possibilities of intervening "hot-spots," or power maxima that may be generated at tissue discontinuities. The general idea, though, is a good one and should be studied further.

In view of the inability to use any frequency of planar electromagnetic radiation to produce a power maximum below the tissue surface, it is clear why this single surface applicator modality is currently used only to treat surface tumors. The solution to this dilemma is to surround the tissue with radio frequency and microwave sources. This can either be done with opposing planar sources [40], perpendicular planar sources [41], or with a cylindrical or even spherical source [42].

d. Planar Arrays

For two infinite, uniform, coherent planar sources, each facing an infinite slab of muscle tissue, the dissipated power yields a significant local maximum at the slab mid-plane. The electrical field distribution is a superposition of two counterpropagating plane waves, each represented by

$$E_{\pm} = \mathrm{Re}\left\{\hat{y}E_0 e^{\mp\alpha z \mp \beta z} e^{j\omega t}\right\} \tag{6}$$

where waves propagating in the positive z-direction follow the upper signs with a complex source value of E_0 at $z = 0$, and in the negative z-direction with the lower signs. Solving for power according to equation (3) gives:

$$P = \frac{\sigma E_0^2}{2}(\sinh^2 \alpha z + \cos^2 \beta z) \tag{7}$$

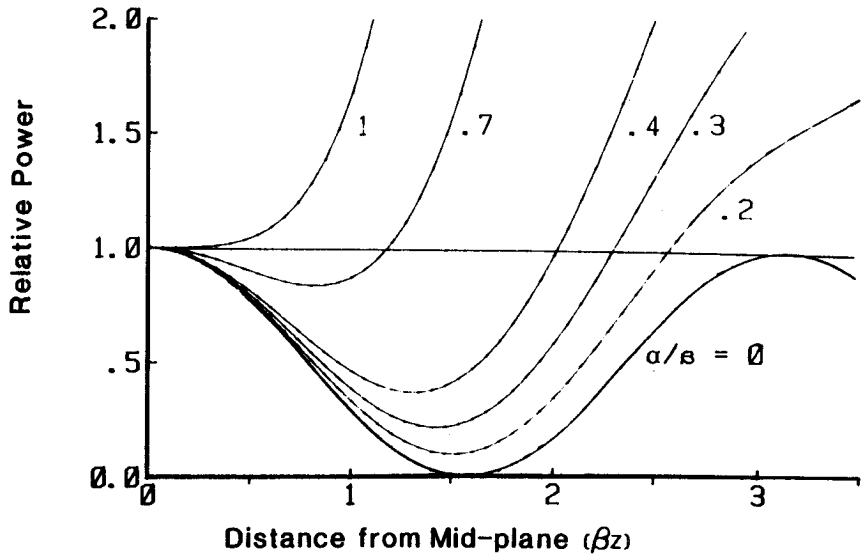

Figure 2.1.3 EM power density distribution normalized to the mid-plane density of an infinite planar slab of thickness $2z$, with uniform coherent source excitation, for typical values of α/β.

The power pattern is depicted in Fig. 2.1.3, where the curve for each value of the ratio α/β is plotted as a function of electrical length, βz, from the mid-plane ($\beta z = 0$) out, and normalized to the power at the mid-plane. The requirement of equal power at the mid-plane and the surface determines the greatest uniform source separation distance. This distance ranges from more than $\beta z = 3.14$ for the lossless case to $\beta z = 1.2$ for $\alpha/\beta = 0.7$. This latter case, $\alpha/\beta = 0.7$, corresponds to a layer of thickness $2.4\lambda/2\pi$. These are universal curves in that frequency and physical dimensions have not yet been specified. The α/β ratios listed in Table 2.1.1 can now be used to determine the appropriate curve in Fig. 2.1.3 to represent the power pattern in actual muscle tissue. The wavelength must also be specified to determine the proper physical scale of slab thickness.

The constructive interference of two opposing uniform sources gives power patterns which are much better than the single source arrangements represented by Fig. 2.1.2. These sources do not make

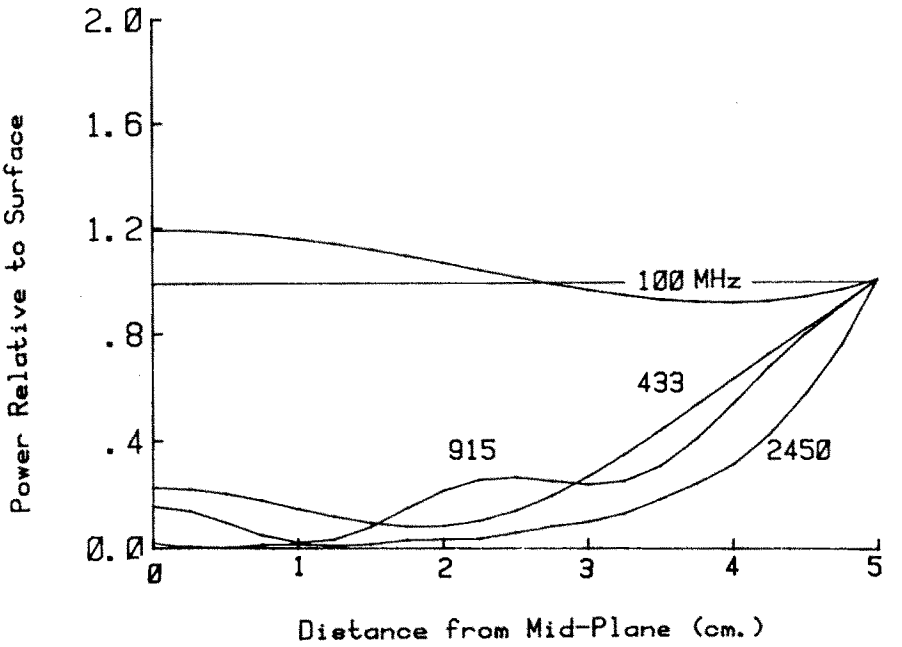

Figure 2.1.4 Power patterns for one half of a 10 cm thick planar slab of muscle tissue, normalized to the power at the surface.

use of phase adjustments to focus on a particular target; rather, they simply produce standing wave maxima in the lossy slab. These curves also indicate the very limited flexibility of constructive interference.

Figure 2.1.4 shows several of these same curves normalized to a surface 5 cm from the mid-plane with a physical distance scale. A 915 MHz arrangement could only be used with slabs less than 3.4 cm thick. For a slab 10 cm thick even the 433 MHz frequency is too high to safely heat the center.

The best method for designing opposing planar arrays is to start with the assumption that power on the tissue surface should be uniform and equal to the maximum tolerable level. Because of the strong exponential decay in muscle tissue, the source surfaces tend to have the greatest deposited power. When this level is the same as that at the focus, the tissue slab thickness is maximum.

e. Circular Cylindrical Arrays

Circular geometry admits wave equation solutions in terms of Bessel functions. The field due to a uniform, axially polarized electric field source on the surface of an infinite cylinder, as depicted in Fig. 2.1.5, is represented by

$$E(\rho) = \hat{z}\,\mathrm{Re}\left\{E_0 I_0[(\alpha + j\beta)\rho]e^{j\omega t}\right\} \tag{8}$$

where I_0 is the zeroth-order modified Bessel function, which grows with increasing ρ. This equation corresponds to (6) from the Cartesian geometry, with polarization changed to align with the z-axis. Figure 2.1.6 is the corresponding set of power patterns, similar to Fig. 2.1.3, but with up to four times the maximum allowable penetration thickness. The curves are spread apart more for low α/β values than with the planar case. This is due to the enhanced phase effects of higher frequency waves. Just as in the case with constructively interfering planar source, the larger wavelengths do not interfere to the same degree over the tissue volume as do smaller wavelengths. At 915 MHz, a uniform infinite cylinder of muscle tissue 6.3 cm in radius can have as much power deposited on its axis as on its surface.

The curves of Fig. 2.1.6 are useful for visualizing overall pattern resolution and maximum cylinder radius determination. For a more practical, physical picture, an unnormalized radial scale must be used. Figure 2.1.7 shows the deposited power patterns within a muscle tissue cylinder of typical adult torso radius of 14 cm for various frequencies. The power is normalized to that at the cylinder surface. Note that the highest frequency depicted, 433 MHz, has insignificantly little power at the axis, $\rho = 0$. For a cylinder as large as 14 cm, the higher frequencies simply cannot be used. Instead, resolution must be sacrificed in favor of penetration, and the 41 MHz frequency choice is optimal. It is not necessary to use a frequency as low as 27 MHz. For this choice, the power level is higher at the axis than at 14 cm. While the lower frequencies cannot provide for a high resolution narrow spot at the tumor, they can still be used for a uniform baseline heating, with another modality, such as ultrasound, used to heat the tumor a few remaining degrees into the therapeutic range.

There is much more literature on pattern synthesis in the cylindrical geometry than with the planar geometry [43–46]. Actual phase and

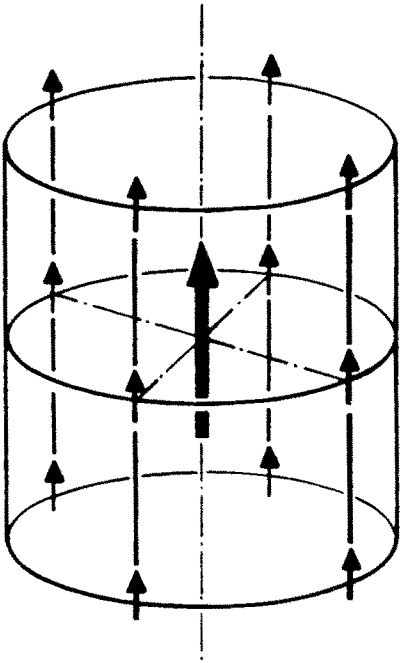

Figure 2.1.5 Electromagnetic polarization alignment for cylindrical source focussing.

amplitude optimization for focussing at various positions throughout the cylinder is also examined [47–49]. Arcangeli et al. [48] and Morita et al. [49] both use a method of optimizing a weighted sum error function. In each case, the tissue volume is assumed to be two-dimensional. The calculated and desired intensity values are determined for several sample points throughout the tissue volume and this error is minimized by least squares. Archangeli then repeats the process by relaxing the limits of the desired power pattern iteratively until the error is minimized. Although this method yields good results, great care must be used in choosing an appropriate desired pattern and sampling grid. An overly optimistic pattern may not be realizable, while a poorly specified grid may either miss fine pattern details or be computationally excessive. Another difficulty is that iterative solutions may not converge, or may converge to a non-physical solution. The Morita paper uses a simplified model of the human torso cross section for their synthesis. Using only uniform muscle, a circular bone region and several

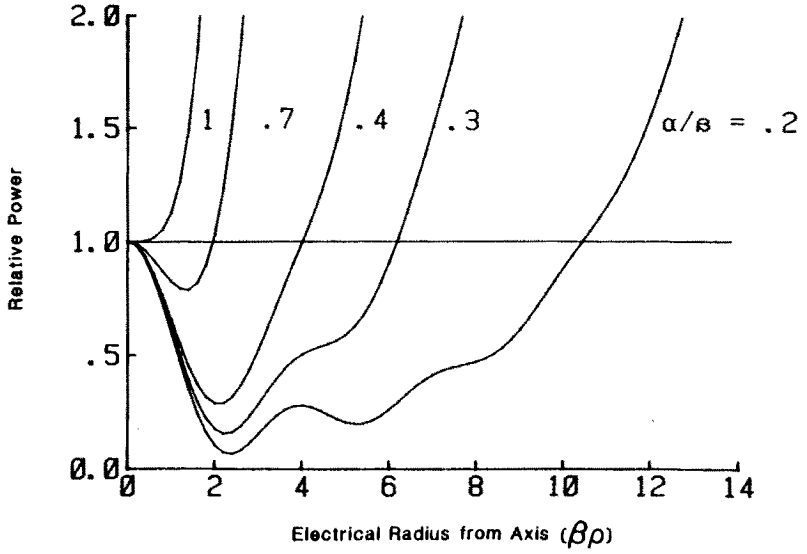

Figure 2.1.6 EM power density distribution normalized to axis density for cylinder of radius ρ with uniform source excitation for typical values of α/β.

circular air-filled bowel regions, with 41 MHz radiation, their derived power patterns are fairly smooth. The authors conclude that because of the transverse polarization of the electric field, the inhomogeneities do not significantly effect the pattern. This important conclusion implies that it may be more useful to optimize the sources for a uniform tissue volume first, and then perturb the results to accommodate the fine structural inhomogeneities.

Arcangeli [48] takes the opposite view by breaking the torso cross section up into discrete regions, each with a representative complex dielectric constant. Using 915 MHz demands a much finer sampling grid, since the sample points must be less than one-half wavelength apart, and a body structure may have a width of 15 wavelengths. The computational expense is much higher for higher frequencies. Although the method is rather sophisticated, the results show focussing very near the surface, with a derived excitation of only 8 of the 50 discrete sources. In other words, the full constructive interference effect of the full cylindrical aperture is ignored in favor of a 60° sector near the

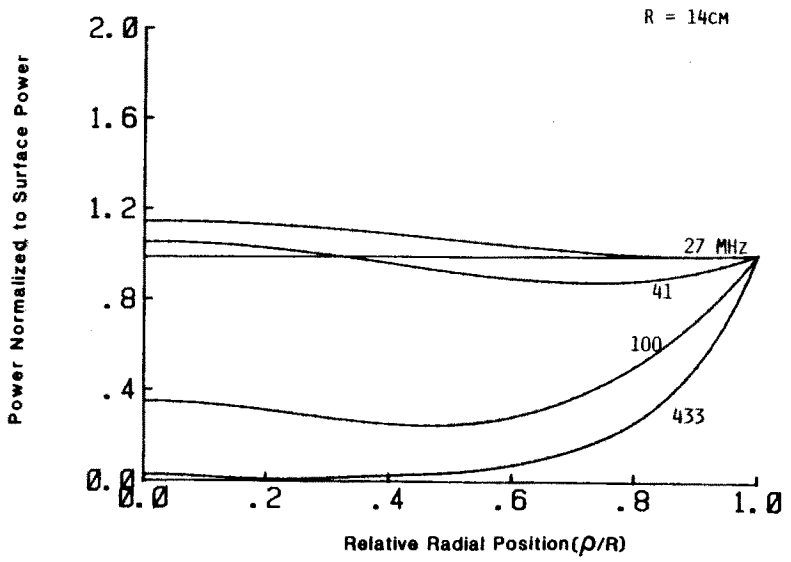

Figure 2.1.7 Power patterns for a 14 cm radius cylinder of muscle tissue normalized to the power at the surface.

region of greatest curvature.

The concept of three dimensional focussing with a cylindrical geometry is fairly new. In a paper by Jouvie et al. [50], the source is focussed in both ϕ- and z-directions. The polarization choice is E_ϕ, lowering the possible efficiency compared to E_z and only a small sector of the neck is irradiated, but their results show a considerable improvement over the uniform source case.

Much work has been done on the Annular Phased Array (APA) system [47], [51–57]. Perhaps the most thoughtfully designed and clinically tested applicator system, the APA uses the entire cylindrical surface surrounding a tissue volume, maintains an axial (z-directed) polarization, and has the capability of rudimentary phase and amplitude adjustment. The APA consists of one or two sets of eight dielectrically loaded, flared, parallel plate TEM waveguides, each facing the cylindrical tissue volume. The edge fringing effects of the TEM wave launchers and the eight plane-wave approximations to a true circular source yield a power pattern slightly worse than the ideal represented by Fig. 2.1.6.

The APA's rudimentary phase control and low frequency operation make it less useful for steering the point of maximum interference throughout the tissue volume. However, it is significantly more flexible than the helical coil applicator [54] which cannot be adjusted after construction.

One more issue not previously considered with the APA system is that of focussing in the axial direction. For maximum power on axis, circumferential distribution is set at uniform phase and amplitude. Adjustments in the axial variation take advantage of the only remaining degree of freedom. This variation is conceptually similar to the planar focussing in the previous section. Amplitude at the source is held constant and the phase is adjusted to compensate for both the electrical path length to the focal point and the complex propagation constant of the medium. The details of this optimization are mathematically presented in section 2.4.

2.2 Optimal Source Distribution for Spherical Tissue Geometry

In section 2.1, it was shown that using various schemes to allow waves to interfere constructively produce much better results than merely radiating from a single, unfocussed applicator. Specifically, surrounding a volume of tissue with sources produced localized maxima in the center. The question arises as to the maximum size of any volume for which as much power can be deposited in the center as elsewhere. This chapter answers this question and presents the optimum source distribution function. It will be demonstrated that the optimum geometry for power generation at depth is a sphere, and that with proper focussing, the maximum penetration depth represents a fundamental heating limit.

In contrast to several previously reported studies, the current examination considers the synthesis of the particular best distribution. A large amount of work has been done analyzing the power pattern in a sphere illuminated by a plane wave [58–60]. For this scattering problem, the deposition pattern is unsymmetrical, since power is incident from only one side. Placing sources on all sides — in effect surrounding the sphere with sources — makes use of the entire aperture and there-

fore provides the greatest constructive interference at the center. The symmetric distribution synthesized has a much greater focal-point-to-surface distance than the plane wave pattern. The optimal synthesis problem, though conceptually more complex, is less computationally difficult than the plane wave scattering analysis, which is usually solved using numerical approximations. Since the former specifies a source polarization, phase and amplitude distribution on the sphere surface, it is not easily analyzed using ray paths or wave fronts. However, since the solution is ultimately determined in terms of spherical harmonics, it is specified in closed form.

There are relatively few biological structures which can be modelled by the spherical geometry. The head (with adequate eye protection) and the breast, making use of the higher conductivity muscle "ground plane" backing layer, are possible candidates. Despite the limited applications, knowledge of the absolute maximum heating depth provides a rule of thumb which specific microwave applicator designs might strive to approach, but never exceed.

a. Lossy Sphere Field Solutions

Since attenuation in dissipative media is roughly exponential with depth, the volume geometry most suitable for maximum constructive interference is one which minimizes the distance from a focal point to the source on its surface. By this criterion, a sphere is optimum, since any other volume can always be inscribed by a sphere. Thus, given the minimum focal point to surface distance R and the maximum tolerable surface power, a sphere of radius R will yield the greatest power maximum at that focal point, the origin.

The polarization of the source on the surface of the sphere is another important characteristic. As shown in Fig. 2.2.1, it must be parallel to some axis, say the z-axis. By symmetry, these z-directed source components are independent of circulating angle (ϕ), and have polar angle (θ) dependence which is symmetric about the equator $(\theta = \pi/2)$. Any additional radially symmetric (r) polarization component cancels itself at the center, whereas any circulating component vanishes there. An additional polar angle component can be decomposed into an antisymmetric radial component and a z-directed component for overall power pattern imrovement, and may be a desirable

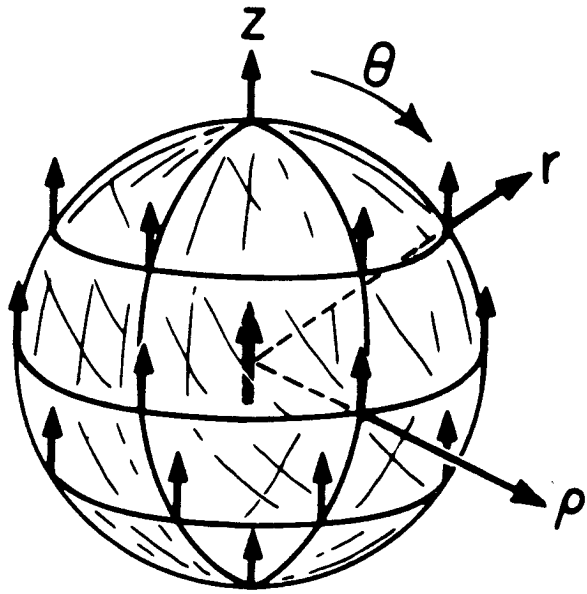

Figure 2.2.1 Currents polarized in the z-direction on the surface of a sphere, and the resulting maximum constructive interference of electric field at the center.

component, but cannot be easily used for preliminary source synthesis. If possible, the first step for a source design would be to maintain polarization parallel to the z-axis.

Specifying the optimal phases and amplitudes of these source components is the next step in this derivation. Contrary to established intuition, the best focussed source distribution is not uniform amplitude and phase, as it would be for an acoustic compression wave. To examine the deficiencies of this uniform distribution, we first solve the surface current diffraction integral and then improve this solution using a modal analysis to yield the optimum distribution.

The uniform z polarized surface current at a radius R is represented as

$$\overline{J}(\overline{r}') = \delta(r - R)\hat{z}$$

where $\delta(r)$ is the three-dimensional spatial impulse function. This cur-

rent is inserted in the dyadic Green's function diffraction formula [61]

$$\overline{E} = -j\omega\left(\overline{\overline{I}} + \frac{1}{k^2}\nabla\nabla\right)\cdot\overline{A}(r) \tag{1}$$

$$\overline{A}(r) = \mu\int_{V'} dv' \frac{e^{-jk|\overline{r}-\overline{r}'|}}{4\pi|\overline{r}-\overline{r}'|}\overline{J}(\overline{r}') \tag{2}$$

where the left hand side of (1) is the vector electric field at the observer point $\overline{r}$, $\overline{A}(\overline{r})$ is the vector potential, ω is radian frequency, $\overline{\overline{I}}$ is the identity dyadic, $k = \beta - j\alpha$ is the complex wave number, and $|\overline{r}-\overline{r}'|$ is the observer-to-integration-point distance. The law of cosines is used to represent $|\overline{r}-\overline{r}'|$, where $\overline{r}$ is assumed to lie on the z-axis. This assumption is justified since the source is uniform and symmetric and the only requirement on polarization is that it is parallel to any arbitrary axis. That is , the vector potential $\overline{A}$ is independent of observer coordinates θ and ϕ. As would be the case with a scalar wave, $\overline{A}$ represents a family of concentric, spherical equipotentials-potentials. The source polarization enters only as a linear multiplier to this scalar function. The integral in (2) becomes a surface integral

$$\overline{A}(r) = \mu\int_0^{\pi} d\theta' \int_0^{2\pi} d\phi' R^2 \sin\theta' \frac{e^{-jk\sqrt{R^2+r^2-2rR\cos\theta'}}}{4\pi\sqrt{R^2+r^2-2rR\cos\theta'}}\hat{z} \tag{3}$$

which is readily integrated, giving

$$\overline{A} = \hat{z}\frac{\mu}{2}\left(\frac{R}{-jkr}\right)\left(e^{-jk|R+r|} - e^{-jk|R-r|}\right) \tag{4}$$

Inside the sphere, $r < R$, the vector potential can be represented by a spherical Bessel function of radial position, $j_0(kr)$,

$$\begin{aligned}\overline{A}(r) &= \hat{z}\mu\,\Re\left\{e^{-jkR}\frac{\sin kr}{kr}\right\} \\ &= \hat{z}\mu\,\Re\left\{e^{-jkR}j_0(kr)\right\}\end{aligned} \tag{5}$$

It is at this point that the vector nature of the electromagnetic field presents itself. Substituting this expression back into (1) and taking

derivatives in cylindrical coordinates, (ρ, ϕ, z), give

$$\overline{E}(z,\rho) = -j\omega\mu\,\Re\left\{e^{-jkR}\left\{\hat{z}\left[\left(\frac{\rho}{r}\right)^2\left(j_0(kr) - \frac{j_1(kr)}{kr}\right)\right.\right.\right.$$
$$\left.\left.\left. + \left(\frac{z}{r}\right)^2\left(2\frac{j_1(kr)}{kr}\right)\right] + \hat{\rho}\left(\frac{z\rho}{r^2}\right)\left[-j_0(kr) + 3\frac{j_1(kr)}{kr}\right]\right\}\right\} \quad (6)$$

with

$$r = \sqrt{z^2 + \rho^2}.$$

Several features of (6) are worth mentioning. First, there is the addition of the ρ-component, and the z-component has three terms instead of just one (as might be expected for a scalar field). Second, for small values of radius, since $j_0(kr) \sim 1$ and $j_1(kr) \sim kr/3$ [62], the electric field simply reduces to

$$\overline{E}(z,\rho) \approx -\hat{z}j\omega\mu\,\Re\left\{\frac{2}{3}e^{-jkR}\right\}$$
$$\approx \hat{z}\left(-j\frac{2}{3}\right)\eta k\,\Re\left\{e^{-jkR}\right\}, \quad kr \ll 1 \quad (7)$$

Next, for large values of radius $|j_n(kr)| \sim |\sin(kr + \frac{n\pi}{2})/kr|$ [63], so (6) becomes

$$\overline{E}(z,\rho) \sim -j\eta k\,\Re\left\{e^{-jkR}j_0(kr)\frac{\rho}{r}\left(\hat{z}\frac{\rho}{r} - \hat{\rho}\frac{z}{r}\right)\right\}, \qquad kr \gg 1 \quad (8)$$

Note that in (8), there is an appreciable E_ρ component away from the equator. Thus, even though the surface currents are polarized parallel to the z-axis, it is recognized that the resulting E-field for large radii is primarily polarized in the $\hat{\theta}$-direction. Equation (8) is no longer valid near the poles where $\rho \approx 0$. Reconsidering (6), again for small ρ gives

$$\overline{E}(z,\rho) \sim -j\eta k\,\Re\left\{e^{-jkR}\left(\hat{z}\,2\frac{j_1(kr)}{kr} - \hat{\rho}\,k\rho\frac{j_0(kr)}{kr}\right)\right\}, \quad \rho \ll z \quad (9)$$

Equation (9) indicates that there exists normal z-directed electric field components at the poles, but that these are $1/kr$ times smaller than the tangential field near the equator.

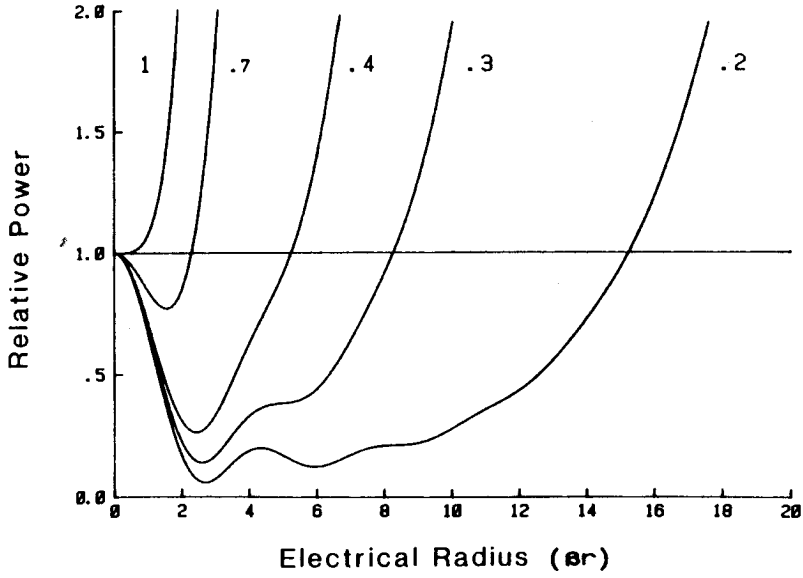

Figure 2.2.2 EM power density distribution normalized to axis density for a sphere of radius r for typical values of α/β.

The dissipated power in a medium of conductivity σ is $\sigma|E|^2/2$. From (8), this is

$$P(z,r) = \frac{\sigma\eta^2}{2}|kr|^2 e^{-2\alpha R}|j_0(kr)|^2 \left(\frac{\rho}{r}\right)^2 \tag{10}$$

which is maximized at $z = 0$, $\rho = r$, at the equator. The exact power deposition function, based on (6) normalized to the power at the origin, is computed and plotted as a function of radius at $z = 0$ in Fig. 2.2.2. These curves are of the same type as the previous universal dimensionless curves. Figure 2.2.3 plots the same set of data on a centimeter scale for several standard frequency values. It is the intersection of each curve with unity which determines the maximum allowable sphere radius. As expected, the lowest frequency curve has a greater penetration depth due to its larger physical wavelength; whereas the higher frequency patterns have much greater resolution with a rather narrow peak at the origin for 2450 MHz. An interesting anomaly exists for 915 MHz, where the penetration depth is actually greater than for 433 MHz. This

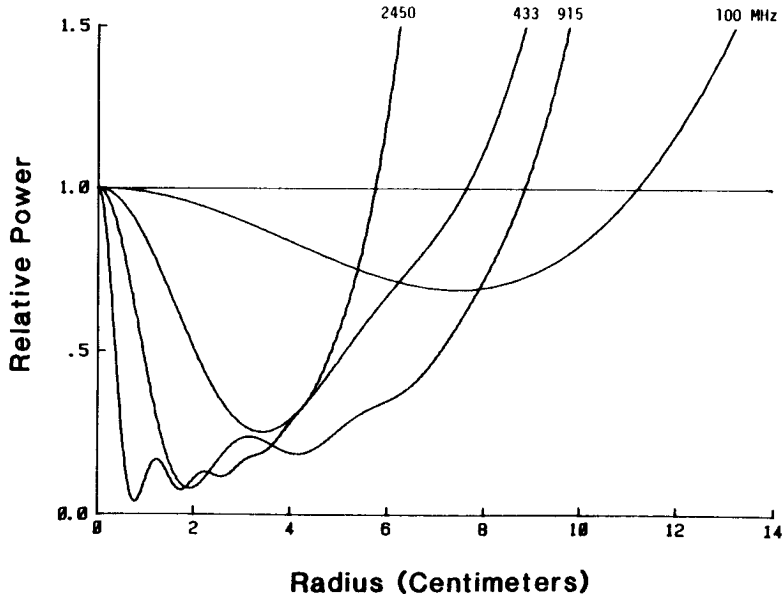

Figure 2.2.3 Power in a sphere of muscle tissue as a function of radius at $\theta = \pi/2$ for four standard hyperthermia frequencies: Uniform current distribution.

is due to the more prominent constructive and destructive phase effects for the higher frequency.

For a given (large) radius, the power varies as $\sin^2\theta$. Arising from the $\sin\theta$ dependence of the infinitesimal element of spherical area, this indicates a much higher power deposition at the equator than at regions near the poles. This can be understood intuitively by considering the limiting cases of planar current distributions on the surface of a sphere of infinite radius. The equatorial positions degenerate to tangential planes of current, while the polar positions degenerate to planes of normal currents, which do not radiate.

The $\sin^2\theta$ non-uniform surface power distribution is corrected using modal analysis in the next section to yield the optimum vector wave solution to the power deposition problem.

To test the error incurred with the assumption of large radius made for (8) for the worst case, 433 MHZ, where the maximum radius is approximately $.9\lambda$, $|kr| = 6.3$, the neglected power, as given by

computing the squared magnitude of the electric field in (9), is of the order of 4% at the pole. For 915 MHz, this error is only about 1%.

b. Modal Analysis

Solutions to the wave equation for spherical geometry are harmonics of index n, represented by [64]

$$\overline{E}(r) = \sum_{n=1}^{\infty} \left\{ \hat{r} A_n \frac{n(n+1)}{kr} j_n(kr) P_n(\cos\theta) + \hat{\theta} A_n \left[j_{n-1}(kr) - \frac{n}{kr} j_n(kr) \right] \right.$$
$$\left. \cdot [n \cos\theta P_n(\cos\theta) - n P_{n-1}(\cos\theta)] \left(\frac{1}{\sin\theta} \right) \right\} \tag{11}$$

where P_n is the Legendre polynomial of order n, and A_n is the constant of the nth harmonic. By setting n equal to 1, $A_1 = -j\omega\mu Re^{-jkR}$, and recalling that $P_0(\cos\theta) = 1$ and $P_1(\cos\theta) = \cos\theta$, it is evident that (6) is the first harmonic spherical wave solution as given by (11).

It is the fundamental point of this analysis that for higher order harmonics, $n = 2, 3, 4 \cdots$, the E-field at $r = 0$ vanishes. Since $j_n(kr)$ varies as $(kr)^n$ for small r, these spherical Bessel functions approach zero at the origin. Only the first harmonic, with $j_0(kr)$ and $j_1(kr)/kr$ factors, remains non-zero there, taking the form of (7). This property will now be used to reduce undesirably high power levels at the surface of the sphere without affecting the power at the origin. Specifically, a distribution can be synthesized from these higher order modes with appropriately chosen phase and amplitude to partially cancel the first order mode field at the surface, near the equator, and thereby increase the maximum sphere size.

Once again, for large radius values, the θ-component of E-field is the dominant contribution to the dissipated power function. The θ-dependence of the nth mode of E_θ can be expressed as

$$E_{\theta n}(\theta) \sim \hat{\theta} \frac{\partial P_n(\cos\theta)}{\partial\theta} \tag{12}$$

Since for even order n, $P_n(\cos\theta)$ is an even function of $\cos\theta$, its derivative will be an odd function of $\cos\theta$, with a total value of zero at $\theta = \pi/2$. Since the goal is to find the harmonics with non-zero

values at the equator to be subtracted from the $\sin\theta$ dependence of the first harmonic. Thus only odd order harmonics need be considered for this optimization.

The derivatives of Legendre polynomials comprising the first three odd harmonics are, from (12)

$$\begin{aligned} E_{\theta 1} &\sim -\sin\theta \\ E_{\theta 3} &\sim -\frac{15}{2}\cos^2\theta\sin\theta + \frac{3}{2}\sin\theta \\ E_{\theta 5} &\sim -\frac{315}{8}\cos^4\theta\sin\theta + \frac{105}{4}\cos^2\theta\sin\theta - \frac{15}{8}\sin\theta \end{aligned} \tag{13}$$

with values -1, $3/2$, and $-15/8$, respectively, at $\theta = \pi/2$.

The three equations in (13) can be rewritten in terms of sines of odd multiples of θ

$$\begin{aligned} E_{\theta 1} &\sim -\sin\theta \\ E_{\theta 3} &\sim -\frac{15}{8}\sin 3\theta - \frac{3}{8}\sin\theta \\ E_{\theta 5} &\sim -\frac{315}{128}\sin 5\theta - \frac{105}{128}\sin 3\theta - \frac{30}{128}\sin\theta \end{aligned} \tag{14}$$

The θ-dependence of the sum of the three harmonics from (10) may now be represented by

$$f(\theta) = \sin\theta + B_1\sin 3\theta + B_2\sin 5\theta \tag{15}$$

where B_1 and B_2 are selected to minimize the maximum value of power, $[f(\theta)]^2$, over the domain $0 \leq \theta \leq \pi$. Solving this transcendental formula interactively yields $B_1 = .2365$, and $B_2 = .0640$. The resulting surface power variation has three equal peaks of .685 at $\theta = .294\pi$, $.5\,\pi$, and $.706\,\pi$.

Note that a standard infinite Fourier series composed of higher odd harmonics of the fundamental $\sin\theta$ can produce a square pulse of height $\pi/4$, giving a power (amplitude squared) of .617. However, for any finite sum of Fourier terms, there is always a Gibbs Phenomena at the step edge increasing the amplitude by a factor of about 1.09. This would increase the maximum power to .733, which is greater than the previously derived maximum.

What remains is the derivation of the actual mode amplitudes and phases which multiply each harmonic so that their sum equal $f(\theta)$. Define $\mathcal{J}_n = A_n[j_{n-1}(kR) - (n/kR)j_n(kR)]$ as the multiplicative constant of E_θ from (11) for a given sphere radius R. Then, combining the three equations (14) into the form of (15) gives the system:

$$\begin{aligned} \mathcal{J}_1(-1) + \mathcal{J}_3\left(-\frac{3}{8}\right) + \mathcal{J}_5\left(-\frac{30}{128}\right) &= 1 \\ \mathcal{J}_3\left(-\frac{15}{8}\right) + \mathcal{J}_5\left(-\frac{105}{128}\right) &= B_1 \\ \mathcal{J}_5\left(-\frac{315}{128}\right) &= B_2. \end{aligned} \tag{16}$$

The solution is $\mathcal{J}_1 = -.9509$, $\mathcal{J}_3 = -.1148$, and $\mathcal{J}_5 = -.0260$.

Although the third and fifth order modes do not contribute to power at the origin of the sphere, the first order mode is slightly reduced in order to compensate for the small $\sin\theta$ contributions in these higher modes. Thus, the amplitude in the center is reduced to $-.9509$ of the uniform current value. Renormalizing the coefficients to $\mathcal{J}_1' = 1$, $\mathcal{J}_3' = .1207$, and $\mathcal{J}_5' = .0288$ compensates for this reduction. The surface power is plotted in Fig. 2.2.4, along with the uniform current power. The peak power level is reduced to .757 of the single mode power. The magnitude of the ripple is about $\pm 1.5\%$. Addition of higher order terms would reduce the ripple and lower the maximum surface power slightly. The maximum improvement would be less than 2%, and since from Fig. 2.2.2, the increase in maximum allowable radius varies approximately logarithmically with power, the minute increase in radius does not justify the additional computational complexity required for seventh and higher order harmonies.

Finally, the coefficients A_n from (11) are determined from the $\mathcal{J}_n'$ constants and the magnitudes and phases of the spherical Bessel functions at the unity crossing points of the power pattern for each frequency. Since the pattern changes for each choice of the A_n set, this is an iterative process. For 915 MHz, $A_1 = 1.5e^{j(.6368)}$, $A_2 = 1.364\,e^{j(-2.8608)}$, and $A_3 = 1.136\,e^{j(-.3618)}$, determined at $\beta R = -13.2$, or $R = 9.45$ cm.

The power patterns at $\theta = \pi/2$, for the same frequencies as before are plotted in Fig. 2.2.5. Note the increases in maximum allowable

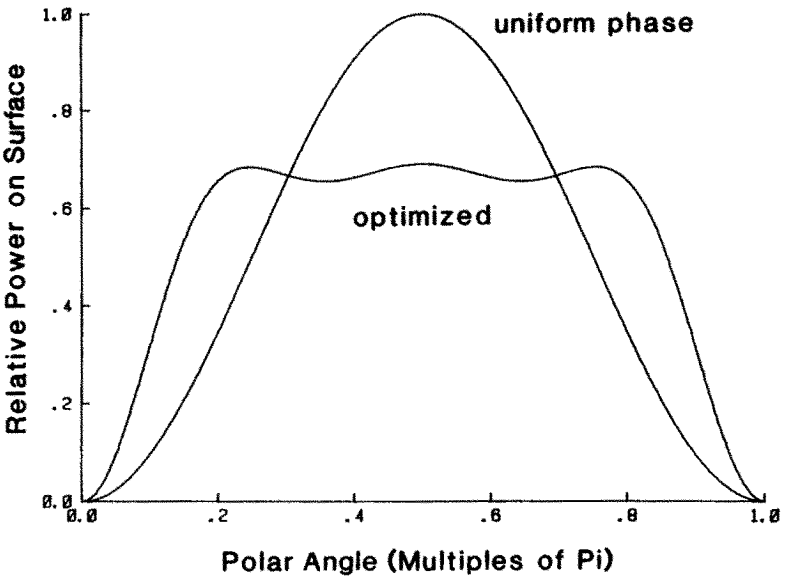

Figure 2.2.4 Surface power as a function of θ for single mode (uniform current) and three modes (approximate uniform power) distributions.

radius, as indicated by the intersection points for the uniform current distribution, taken from Fig. 2.2.2. For 100, 433, 915, and 2450 MHz, the increases amount to 1.72, 0.84, 0.57, and 0.32 cm., respectively.

From (11), it can be seen that for the large radius dominant E_θ term, the radial and polar angle dependencies are separable. Thus, the $\hat{\theta}$-directed power behavior always has the same shape as Fig. 2.2.5 scaled by the θ-dependence of Fig. 2.2.4. Figure 2.2.6 plots the same power curves normalized to the power on the surface at a radius of 9.45 cm. These curves represent the total ($\hat{r}$- and $\hat{\theta}$-directed) power taken at $\theta = \pi/2$. For all other angles except $\theta \approx 0, \pi$, the curves would be similar, with the levels at $r = 0$ and $r = 9.45$ cm being the same as at $\theta = \pi/2$. Note the superiority of the 915 MHz curve both in penetration and resolution.

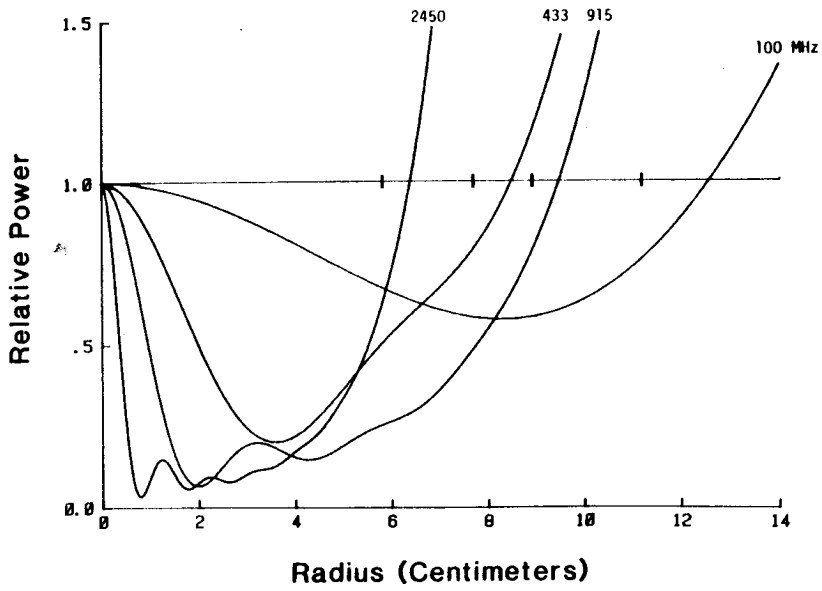

Figure 2.2.5 Power in a sphere of muscle tissue for approximate uniform surface power distribution.

c. Summary

The preceeding discussion has determined the dimensions of the largest convex volume of muscle tissue which can be efficiently heated non-invasively. Constraints have been imposed such that as much power is deposited in the center as elsewhere in the volume or on its surface. These limits are the theoretical best cases (within 1.5%): it is not possible to improve on them by altering the surface phase or amplitude distribution. For other tissue geometries, the maximum penetration depth will, of course, be lower. Although the determination of heating patterns depends on the thermal characteristics of the tissue which are governed by the bio-heat equation, it is reasonable to assume that this solution is also the best for heating the center without overheating any intervening tissue. Heating pattern improvements are possible by making use of surface cooling, but this effect is limited to a few millimeters *in vitro*, or to several centimeters in living animals [65].

The novel aspect of this problem is the vector nature of the source.

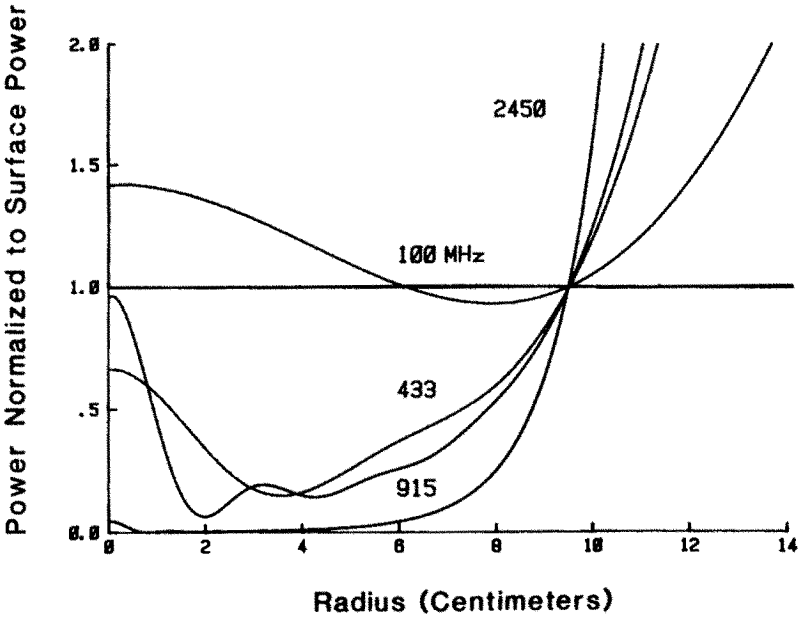

Figure 2.2.6 Power pattern for a 9.45 cm radius sphere of muscle tissue, normalized to the power at the surface.

For scalar waves, such as acoustic waves, the uniform surface excitation would be optimal. For electromagnetic waves, however, polarization is an essential consideration. The method of adding additional modes which do not contribute to power in the center simultaneously provides for adjustments to amplitude, phase, and polarization of the source.

The power optimization makes use of just the θ-component of electric field. As mentioned for the large radii spheres being considered, the radial field contribution is more than an order of magnitude smaller than the tangential $\hat{\theta}$-directed component. Upon squaring the field magnitudes, the radial components contribute only 1% to the surface power, only at the poles (where the tangential contribution is zero). Thus on the sphere surface, the *total* power behavior can be well represented by $|E_\theta|^2$.

This optimization makes use of only one polarization of electric field. Other surface field distributions which are combinations of rotations of the above formulation can be added to the $\hat{z}$-directed max-

imum at the center. These other combinations will be orthogonal to the original distribution, and hence simply uniformly scale the power curves of Figs. 2.2.5 and 2.2.6. Some amount of rotated field (to form, say, an $\hat{x}$-directed central maximum) may be used to increase the power near the poles up to the same level at the equator. This added power is proportional to the marginal surface area covered by this second source orientation — roughly a $2(0.1\pi)^2/4\pi$ or 0.5% increase.

It is clear, however, that any modifications symmetric to the $\hat{z}$-axis will only worsen the situation. These modifications only provide constructive, $\hat{z}$-directed interference in the manner of the surface distributions discussed herein, yet they will add to surface power, making it too large at some locations. The uniform E_θ surface distribution is the best.

Although penetration depth increases with decreasing frequency below 433 MHz, the resolution of the focal spot at the center decreases. However, due to the non-linear dependence of complex dielectric constant on frequency, increasing the frequency does yield an increase in penetration depth for a limited range, as shown by the plot of 915 MHz power curves. For 433 MHz, $\alpha/\beta = 0.40$, whereas for 915 MHz, $\alpha/\beta = 0.23$. There is a small advantage to using a more uniform power surface distribution than the uniform current distribution. The improvements are more pronounced for the lower frequencies since wavelengths are longer and the slopes of the power curves are shallower. It is clear that for muscle tissue geometries of less than 10 cm radius, 915 MHz is the best standard frequency for a producing a well focussed, high-resolution power peak. Of course, if a larger sphere is to be safely heated electromagnetically, the lower frequencies must be used.

2.3 Optimal Power Deposition in a Planar Slab

The method used for deriving the best power pattern in a planar slab is more elaborate than for the sphere. Despite its simpler geometry, there is no single non-vanishing Cartesian harmonic corresponding to the lowest order spherical harmonic. Every harmonic-mode solution to the rectangular wave equation contributes to the power deposition at the focal target. Instead of using a modal algorithm, a direct integration of the surface field must be used to synthesize the best pattern.

a. Uniform Amplitude Current Method

The most popular approach used to generate radiated electric field is integrating the surface currents across an antenna aperture equation (1) in section 2 [66–70]. Although this equation is easily approximated as a Fourier Transform for large source-to-observer distances, it is intractable in the reactive nearfield. Approximating the integral with a Fourier Transform, as done by Johnson and Guy [22], introduces large errors, particularly near the surface. Only with careful numerical integration can the actual field and power pattern be computed.

The optimization process involves determining the phase and amplitudes of an infinite ensemble of surface currents which maximizes the field amplitude at the focus. This must be done subject to the constraint of keeping the maximum power elsewhere below a specified threshold. The greatest difficulty is that it is not known where in the slab the maxima will occur. From the power pattern of the uniform planar case (Figure 2.1.3), the first assumption would be that maxima would fall close to the planes $\beta z = \pm\pi$, corresponding to one half a wavelength from the focus. Waves from each of these source planes add constructively at the focus. Sources placed along these planes are then assigned modified conjugate phase, corresponding to the negative of the electric path length from the source to the focus at $z = 0$ plus a correction factor for lossy media. The correction is necessary to account for the non-exponential factor in the integrand, which is a function of the wave number k. In lossy media, k is complex, so the true phase of the integrand includes a term equal to the arctangent of the imaginary part divided by the real part of this factor, in addition to the usual electrical distance from source to focus. For a current source with phase opposite to this resulting phase, the integrand is purely real for the observation point at the focus.

It is harder to choose the best source current amplitude distribution than phase distribution. Contrary to intuition, uniform source current amplitude is a poor choice. With non-uniform phase, a uniform amplitude source current does not produce uniform surface power. The contributions from these currents to the electric field on the surface add constructively or destructively depending on the observation position. Figure 2.3.1 shows the wide surface power variation generated by a phase-focussed uniform amplitude current source. The power on the

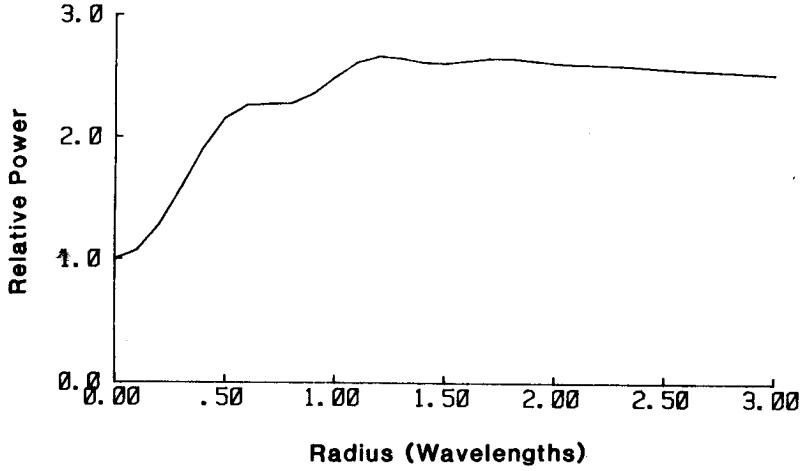

Figure 2.3.1 Radial power distribution at the source surface for focussed surface current.

source planes is plotted as a function of radius from the axis of phase symmetry. Since heating is directly related to dissipated power, it is essential to minimize the maximum power peaks on the source surfaces to prevent overheating. Also, the lower power levels can be increased to add power at the focus, until they approach the maximum surface power level. Thus, a uniform surface *power* rather than current distribution is desirable. Clearly the almost three-to-one radial variation in power in Fig. 2.3.1 makes optimal synthesis based solely on the power along the symmetry axis ($\rho = 0$) infeasible.

b. Uniform Surface Power Method

Having shown that the uniform amplitude surface current produces non-uniform surface power, it becomes clear that it is very hard to generate an optimum choice.

If instead of specifying the electrical surface current, $\overline{J}$, the surface field, $\overline{E}$, is chosen first, the results are preferable. As with the case of the sphere in section 2.2, it is assumed that the power at the surface is the limiting constraint, and should therefore be made uniform. The only mechanism for power dissipation in biological tissue is

ohmic loss with dependence $\sigma|\overline{E}|^2/2$. It is the electric field that must be optimized. Magnetic currents at the source will either be included in the electric field by the equivalence principle, or will be extraneous. Optimizing just the electric field optimizes the volume power dissipation distribution. Unfortunately, the modal solution for the planar geometry cannot be used for this synthesis.

Alternatively, it is possible to use the Kirchhoff integral formula [61] to generate the electric field everywhere in a half-space bounded by a plane with specified electric field, and having decaying wave solutions which vanish at infinity. By assuming the field on this source plane has uniform amplitude, the synthesis problem reduces to finding the best phase distribution. Determining the phase function is similar to the previously mentioned current case: choose it so as to make the integrand purely real for the observation field-point at the focus. It is considerably more difficult, however, to do this since a non-linear differential equation must be solved.

The integral formula can be written as

$$\overline{E}(\overline{r}) = \int_{A'} da' \left[\overline{E}(\overline{r}') \frac{\partial g(\overline{r}, \overline{r}')}{\partial n'} - g(\overline{r}, \overline{r}') \frac{\partial \overline{E}(\overline{r}')}{\partial n'} \right] \tag{1}$$

$$g(\overline{r}, \overline{r}') = \frac{e^{-jk|\overline{r}-\overline{r}'|}}{4\pi|\overline{r}-\overline{r}'|}$$

where $g(\overline{r}, \overline{r}')$ is the spherical Green's function, $\overline{r}$ is the observer field-point (ρ, z), $\overline{r}'$ is the source field point vector (ρ', z'), $\partial/\partial n'$ is the derivative normal to the planar source surface A' with the normal pointing towards the direction of propagation and $\overline{E}(\overline{r}')$ is the specified electric field on that surface.

For a planar geometry, using cylindrical coordinates with the source plane perpendicular to the z-axis crossing through $z = \mp d/2$, (1) reduces to

$$\overline{E}(\overline{r}) = \int_0^{2\pi} d\phi' \int_0^{\infty} \rho d\rho' \left[\overline{E}(\overline{r}') \left(\pm \frac{\partial g(\overline{r}, \overline{r}')}{\partial z'} \right) - g(\overline{r}, \overline{r}') \left(\pm \frac{\partial \overline{E}(\overline{r}')}{\partial z'} \right) \right]_{z' = \mp d/2} \tag{2}$$

with

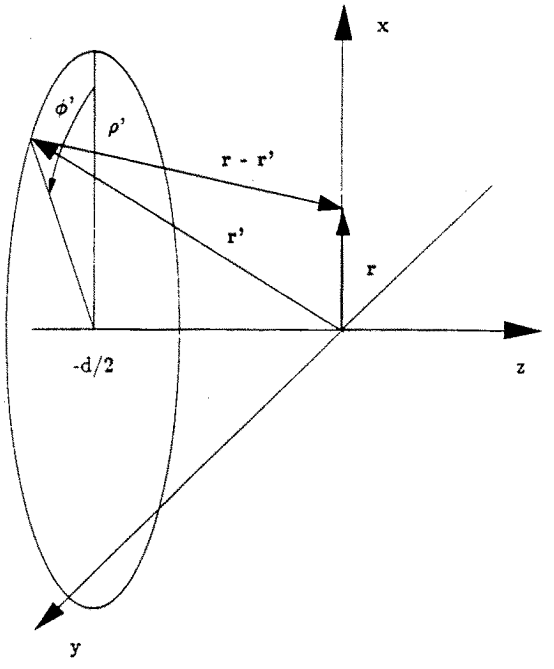

Figure 2.3.2 Coordinate geometry for planar surface integration.

$$|\bar{r} - \bar{r}'| = \sqrt{\rho^2 + \rho'^2 - 2\rho\rho' \cos\phi' + (z - z')^2}\,\Big|_{z'=\mp d/2}$$

Equation (2) is used for both opposing planar sources, with $d/2 + z$ being the distance along the z-axis from observer point z to the source at $z = -d/2$, and $d/2 - z$ for distance from z to the source at $z = d/2$. The normal derivative is chosen to always have the normal point to the origin. The first three terms in the expression for $|\bar{r} - \bar{r}'|$ result from the Law of Cosines, using $\phi = 0$ as the observation point, as shown in Fig. 2.3.2.

To specify the electric field on the source plane, both the tangential (radial) and longitudinal (axial) dependences must be used. Although only the radial dependence of phase exists on the source plane, the normal derivative at the surface requires phase terms proportional to z. Assuming a y-polarized wave with amplitude held constant at unity, the electric field can be represented with a phase function power series

in increasing powers of z

$$\overline{E}(\overline{r}) = \hat{y}\, e^{j\Phi(\rho) - jk_z(\frac{d}{2} \pm z) - jk_{z2}(\frac{d}{2} \pm z)^2 - jk_{z3}(\frac{d}{2} \pm z)^3 - \cdots} \tag{3}$$

where $\Phi(\rho)$ is the surface phase radial dependence at $z = \mp d/2$, and the choice of sign preceding each z is the positive for the source at $z = -d/2$ with wave propagation to the right, and negative for source at $z = d/2$ propagating to the left. The entries into the integral of (2) are

$$\begin{aligned} \overline{E}(\overline{r}') \Big|_{z'=\mp d/2} &= \hat{y}\, e^{j\Phi(\rho')} \\ \pm \frac{\partial \overline{E}(\overline{r}')}{\partial z'} \Big|_{z'=\mp d/2} &= \hat{y}\,(-jk_z) e^{j\Phi(\rho')} \end{aligned} \tag{4}$$

where k_z is yet to be determined.

Using one further identification to simplify notation, $R = |\overline{r} - \overline{r}'|$, the normal derivative of the Green's function is

$$\begin{aligned} \pm \frac{\partial g(\overline{r}, \overline{r}')}{\partial z'} \Big|_{z'=\mp d/2} &= (-jk - 1/R) \frac{e^{-jkR}}{4\pi R} \frac{\partial R}{\partial z'} \Big|_{z'=\mp d/2} \\ &= (jk + 1/R) \frac{e^{-jkR}}{4\pi R} \left(\frac{d/2 \pm z}{R} \right) \end{aligned} \tag{5}$$

c. *Wavefront Determination*

Appealing to the theory of the eikonal for large k, let the wave phase be represented by $L(\rho, z)$. The eikonal equation is then [71]

$$\|\nabla L(\rho, z)\| = k \tag{6}$$

where the double magnitude indicates the complex vector length, or the square root of the inner product with itself. The normal to a constant phase wavefront is

$$\hat{n} = \frac{\nabla L}{\|\nabla L\|} \tag{7}$$

Using the expression for phases in (3) gives

$$\nabla L\Big|_{z'=\mp d/2} = \hat{\rho}\frac{\partial \Phi}{\partial \rho'} - \hat{z}k_z \tag{8}$$

Note that $\partial\Phi/\partial\rho'$ can be defined as $-k_\rho$.

Substituting (8) into (6) yields two equations, the real and the imaginary parts being

$$\begin{aligned} \Phi'^2 + \beta_z^2 - \alpha_z^2 &= \beta^2 - \alpha^2 \\ -2\alpha_z\beta_z &= -2\alpha\beta \end{aligned} \tag{9}$$

where $\Phi' = \partial\Phi/\partial\rho'$ and $k_z = \beta_z - j\alpha_z$.

Solving the two equations of (9) for β_z and α_z gives

$$\begin{aligned} \beta_z^2 &= \frac{\beta^2 - \alpha^2 - \Phi'^2}{2} + \sqrt{\left(\frac{\beta^2 - \alpha^2 - \Phi'^2}{2}\right)^2 + \alpha^2\beta^2} \\ \alpha_z^2 &= -\frac{\beta^2 - \alpha^2 - \Phi'^2}{2} + \sqrt{\left(\frac{\beta^2 - \alpha^2 - \Phi'^2}{2}\right)^2 + \alpha^2\beta^2} \end{aligned} \tag{10}$$

The positive values of β_z and α_z are chosen to give waves propagating toward the focus.

The values of β_z and α_z join $-k_\rho$ to represent the shape of an inhomogeneous incoming wave as it crosses the $z = \mp d/2$ planes. This wave has many features of a spherical wave, and yet it is different in an important way. A spherical wave, far from its source, approaches an e^{-jkr}/r dependence and yields a hyperbolic phase function on the $z = \mp d/2$ surface $\sqrt{\rho'^2 + (d/2)^2}$. This will be shown shortly to be very close to the phase for the currently-addressed focussed solution. However, a spherical wave has a tapering amplitude as well. As seen with the uniform focussed current analysis, improper amplitude choice can lead to unexpectedly bad results.

There are several important features of (10) worth examining. First, consider the behavior of α_z and β_z as Φ' increases from zero (as it will soon be shown to do). Initially at zero, it follows that $\alpha_z = \alpha$, and $\beta_z = \beta$. Alternatively, for large Φ', α_z approaches Φ', and β_z

approaches $\alpha\beta/\Phi'$, which vanishes for infinite Φ'. Furthermore, taking the derivative with respect to Φ'^2 of each equation in (10) results in the pair

$$\frac{\partial\beta_z^2}{\partial\Phi'^2} = -\frac{1}{2} - \frac{\beta^2 - \alpha^2 - \Phi'^2}{2\sqrt{\left(\beta^2 - \alpha^2 - \Phi'^2\right)^2 + 4\alpha^2\beta^2}}$$

$$\frac{\partial\alpha_z^2}{\partial\Phi'^2} = \frac{\partial\beta_z^2}{\partial\Phi'^2} + 1 \tag{11}$$

Setting (11) to zero to find an extremum for α_z or β_z has no real solutions for Φ'. Thus β_z starts at β and decreases monotonically to zero; while α_z starts at α and monotonically increases with increasing Φ'.

Physically, the above mathematics can be interpreted as follows. The attenuation rate in the direction of wave penetration is minimum for a uniform phase distribution ($\Phi' = 0$) with the value of the medium, α. The propagation constant is either the value of the medium, β, for uniform phase, or less for varying phase. Therefore, the penetration wavelength increases for higher spatial frequency variation, $\Phi' > 0$. These two effects, greater attenuation rate and greater wavelength, both conspire to prevent high resolution penetration. In fact, the α_z/β_z ratio — which for non-uniform waves replaces α/β as the relevant pattern parameter — grows much faster with Φ' than with frequency. It can be concluded that the higher the spatial frequency variation of the source phase, the less the wave penetrates the medium. For the optimum source distribution, it would be expected that a majority of the source would have slowly varying phase, with a limitation on the maximum spatial variation. This will next be shown to be the case.

d. Phase Function Solutions

Combining (2), (3), (5), and the notation of (10) gives a revised integral

$$\overline{E}(\overline{r}) = \int_0^{2\pi} d\phi' \int_0^{\infty} \rho' d\rho' \left[j\left(\frac{d/2 \pm z}{R}\beta + \beta_z\right) + \frac{d/2 \pm z}{R}\left(\alpha + \frac{1}{R}\right) + \alpha_z \right] \frac{e^{-j[kR - \Phi(\rho')]}}{4\pi R} \tag{12}$$

for the electric field due to sources on the plane at $z = \pm d/2$. The remaining task is to determine $\Phi'(\rho')$ so that the integral is maximized at the focal point, $(\rho, z) = (0,0)$. This condition occurs when the integrand is entirely real and positive for all values of integration arguments ϕ' and ρ'. The integrand can be written in magnitude/phase form as

$$\frac{\rho'}{4\pi R}\sqrt{\left[\frac{d/2 \pm z}{R}\beta + \beta_z\right]^2 + \left[\frac{d/2 \pm z}{R}(\alpha + 1/R) + \alpha_z\right]^2}$$
$$\cdot \exp\left\{-\alpha R + j\left[-\beta R + \Phi(\rho')\right.\right.$$
$$\left.\left. + \tan^{-1}\frac{\beta(d/2 \pm z) + \beta_z R}{(d/2 \pm z)/R + \alpha(d/2 \pm z) + \alpha_z R}\right]\right\} \tag{13}$$

Setting the imaginary part of the exponent to zero at the focus, $z = 0$, yields the nonlinear differential equation for Φ:

$$\Phi(\rho') = \beta R_0$$
$$- \tan^{-1}\frac{\beta d/2 + \left[\frac{\beta^2 - \alpha^2 - \Phi'^2}{2} + \sqrt{\left(\frac{\beta^2 - \alpha^2 - \Phi'^2}{2}\right)^2 + \alpha^2\beta^2}\right]^{1/2} R_0}{d/2R_0 + \alpha d/2 + \left[-\frac{\beta^2 - \alpha^2 - \Phi'^2}{2} + \sqrt{\left(\frac{\beta^2 - \alpha^2 - \Phi'^2}{2}\right)^2 + \alpha^2\beta^2}\right]^{1/2} R_0} \tag{14}$$

where

$$R_0 = \sqrt{\rho'^2 + (d/2)^2}$$

Equation (14) must be solved numerically. Fortunately, the variations due to the arctangent function are small, so good approximations for small values of ρ' are possible using only the first few terms of a power series. A solution including a term proportional to $1/\rho'$ is needed in the series expansion for large values of ρ'. The blending region between the two series approximations ends up being near a point of inflection of the arctangent function.

Using trial and error adjustments on coefficients a_i, the value of the arctangent is compared to $\Phi(\rho') - \beta R_0$ with the phase approximated by the even power series

$$\Phi(\rho') - \beta R_0 = a_0 + a_1\rho'^2 + a_2\rho'^4 + a_3\rho'^6 + a_4\rho'^8 \tag{15}$$

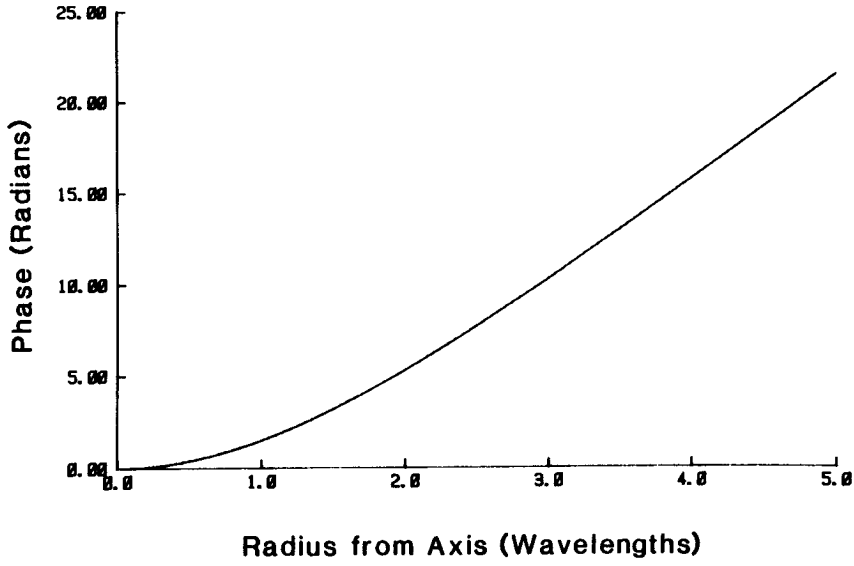

Figure 2.3.3 Phase function for focussing at a point 1.225λ from the source plane, at 915 MHz.

The coefficient a_0 is equal to $-\tan^{-1}[\beta d/(1+\alpha d)]$. Next, starting with a_1, each coefficient is adjusted until the best possible fit occurs. The larger ρ' values are minimized with adjustments to progressively higher order coefficients. After the crossover point, between 1.4 and 3 wavelengths — depending on frequency and $d/2$ — another series of the form

$$\Phi(\rho') - \beta R_0 = b_0 + b_1/\rho' + b_2\rho' + b_3\rho'^2 \tag{16}$$

is used. Table 2.3.1 lists the best phase coefficients and crossover points for several values of $d/2$ at 915 MHz. This frequency is chosen to take the greatest advantage of phase effects without compromising penetration. As shown in section *b* with the sphere analysis, 915 MHz is preferable to both 433 and 1200 MHz. Figure 2.3.3 plots the phase function $\Phi(\rho')$ for $d/2 = 1.225\lambda$ (wavelength), for $0 \leq \rho \leq 5\lambda$ radius. Note that this function is primarily hyperbolic with the functional dependence seen previously. Also, $\Phi(\rho')$ does indeed start from 0 and increases monotonically, as expected. If this hyperbolic term is subtracted out, Fig. 2.3.4 results. This curve corresponds to the addi-

tional effects of the complex amplitude. It is clear that this addition of almost one half a wavelength to the phase must not be neglected. One further plot, Fig. 2.3.5 subtracts the series approximations of $\Phi(\rho')$ (15) and (16) from the resulting $\Phi(\rho')$ given in (14) using the derivatives of these series. This curve shows that the series gives a very good approximate solution to the differential equation (14), with error of only several thousandths of a wavelength.

Table 2.3.1 Phase coefficients and crossover points for complex amplitude integrand.

$d/2$ (λ)	a_0	a_1 $\div$ .01	a_2 $\div$ .001	a_3 $\div$ .001	a_4 $\div$ .0001	b_0	b_1 $\div$ .01	b_2 $\div$ .01	b_3 $\div$ .001	X-pt
1.0	5.0135	1.08	3.5	−2.5	−2.3	4.9765	−0.8	2.81	−3.1	1.2
1.2	5.0014	.88	−.07	−.045	−.21	4.584	−3.4	1.50	−1.2	1.9
1.225	5.0002	.84	.005	−.012	−.35	5.1200	−3.4	1.51	−1.2	2.0
1.25	4.9989	.80	.07	−.045	−.20	5.1129	−3.4	1.52	−1.2	2.1
1.3	4.9967	.765	−.02	−.095	.06	5.1776	−4.7	1.15	−0.8	2.5
1.5	4.9892	.57	.25	−.130	−.10	5.4062	−10.0	−0.001	0.3	2.9
2.0	4.9768	.35	−.02	−.006	0.0	4.7193	2.32	2.47	−1.7	2.5

e. Optimum Planar Power Pattern

With a focussed source, the electric field and dissipated power pattern depend on the thickness of the planar slab. This contrasts with the uniform source examples of section 2.1, where the maximum thickness is selected based on where a particular curve intersects unity. It is difficult to determine the thickest possible slab directly. Instead, this limit must be found iteratively.

Consider first a two-wavelength thick slab, $d = 2\lambda$. Figure 2.3.6 shows the power pattern along $\rho = 0$, the axis of symmetry of the phase function, through the focal point at $(\rho, z) = (0, 0)$. The focussed power at this focal point is 10.4 times greater than for the unfocussed opposing plane case of Fig. 2.1.3, which is redrawn for comparison

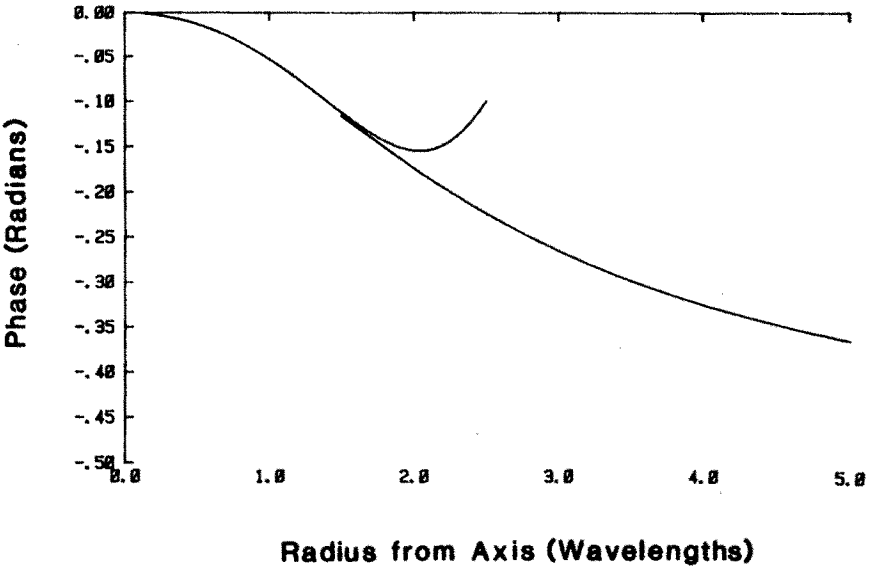

Figure 2.3.4 Correction function for complex integrand amplitude for focussing at 1.225λ depth.

in Fig. 2.3.6 normalized to the power at the source planes. In fact, the power is greater at the focus than anywhere else. The secondary maximum at about one half wavelength from the focus has been moved out to $.67\lambda$ and is only 89% of the focal point power. Whereas this secondary maximum height established the largest slab thickness for the unfocussed example, it is no longer a problem with this particular phase-focussed case. The constructive effects of phase focussing are much less prevalent at points close to the source than at the mid-plane. Already, the maximum thickness has been doubled by using focussing.

Since no part of the power pattern exceeds the focal point level, it is possible to extend the slab thickness even further. An upper limit to the thickness can be extrapolated from the two-wavelength example. If it is assumed that the growth of the focussed power pattern near a source edge behaves like the unfocussed pattern, then it suffices to extend the focussed pattern until it reaches the level of the focal point power. This occurs at a thickness of 2.59λ. Unfortunately, for this thickness, the secondary maximum becomes excessively high — almost 1.3 times the

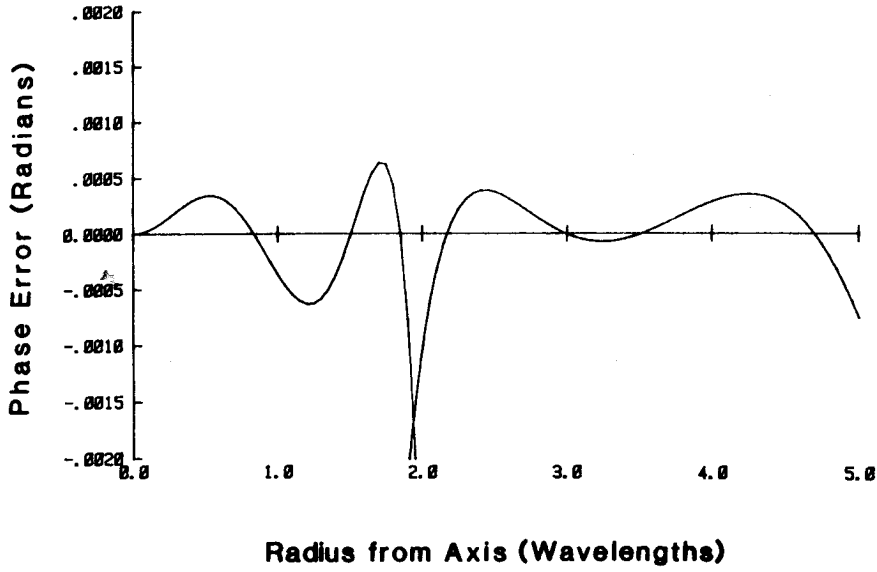

Figure 2.3.5 Approximation error for 1.225λ series.

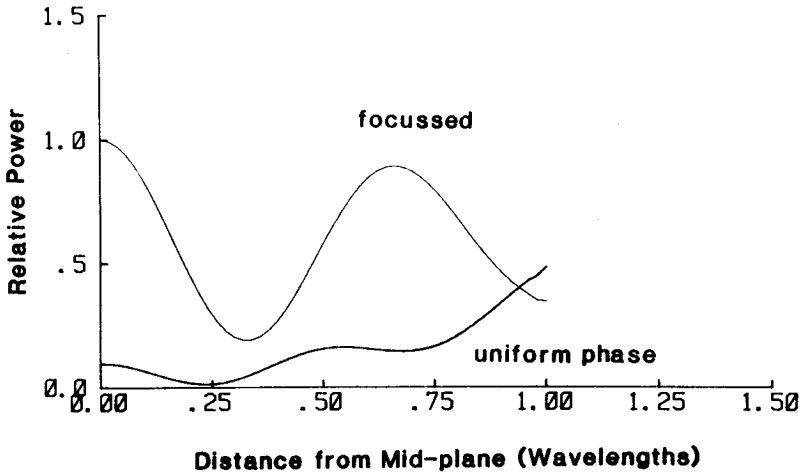

Figure 2.3.6 Power pattern for a focussed 2λ thick planar slab.

level of the focal point power. The rise in this secondary maximum is due to the increase in the constructive interference at this location, now farther from the source. That is, the thicker the slab, the less the hyperbolic phase minus the electrical path length to $(\rho, z) = (0, .67\lambda)$ varies with radial source position. It is concluded that the limiting thickness falls between 2λ and 2.59λ.

There are two competing constraining effects limiting the planar slab thickness: the high power levels at the source surface and at the secondary maximum. This is a different situation from the sphere synthesis, and, as will be shown in the next section, from the focussed cylinder synthesis. An additional optimizing method has been derived to reduce the secondary maximum power level to a greater extent than the focal point power without raising the surface power. The method involves decreasing the amplitude of the source in particular regions. The phase is kept the same as from the above synthesis so that the focus still receives coherent contributions from the entire source. The secondary maximum lies along the axis of phase symmetry, $\rho = 0$, and receives the greatest portion of its power from sources close to this axis. At this secondary maximum, contributions from these closest sources are greater than the non-coherent destructive interference from more remote sources. For observer points farther from the source than this secondary maximum, including, in particular the focus, the path length variations (and hence the exponential attenuation multiplier) are smaller for a given change in ρ. Mathematically, if the source-to-secondary maximum distance is represented by s, it is clear that

$$\left|\sqrt{\rho_1^2 + (d/2)^2} - \sqrt{\rho_2^2 + (d/2)^2}\right| < \left|\sqrt{\rho_1^2 + s^2} - \sqrt{\rho_2^2 + s^2}\right|$$

$d/2 > s$, for any two radial positions $\rho_1 \neq \rho_2$

Thus, if the amplitude is reduced in a narrow region about the $\rho = 0$ axis, the destructive effects of the remote sources become more important. The secondary maximum level will be reduced more than the focal point level. Furthermore, since the source amplitude is only being reduced, there will be no increase in surface power anywhere.

The choice of the amplitude reduction function is somewhat arbitrary. One function that works well is based on a Gaussian, and is

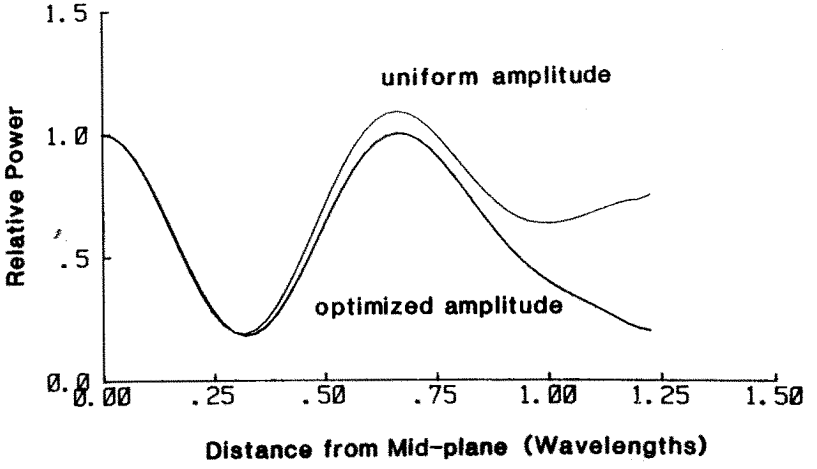

Figure 2.3.7 Focussed unit amplitude and optimal power patterns for 915 MHz focussed planar source.

stated

$$A(\rho) = \frac{1}{1 + ae^{-b\rho^2}} \tag{17}$$

By iterative optimization, the best attainable power is for a planar slab $2.45\,\lambda$ thick, with the amplitude dependence of (17) with $a = 1.0$ and $b = 7$. It is interesting to note that this amplitude variation is in the opposite manner to that of a spherical wave, discussed previously. Optimization involves testing a set of a and b parameters to obtain the largest focal point power while simultaneously keeping the secondary maximum below this power level. In general, as a increases the power is reduced at both positions, while decreasing b causes a preferential reduction of the secondary maximum power level. If despite all combinations of a and b the greatest value of focal point power is still below either the highest source surface power level or the secondary maximum power level, the thickness must be reduced. The effects of the second opposing source on a source surface must be taken into account when computing the power there. The power is proportional to the square of the sum of $A(\rho)$ and the intensity from the other source. The unit amplitude pattern and adjusted amplitude pattern are plot-

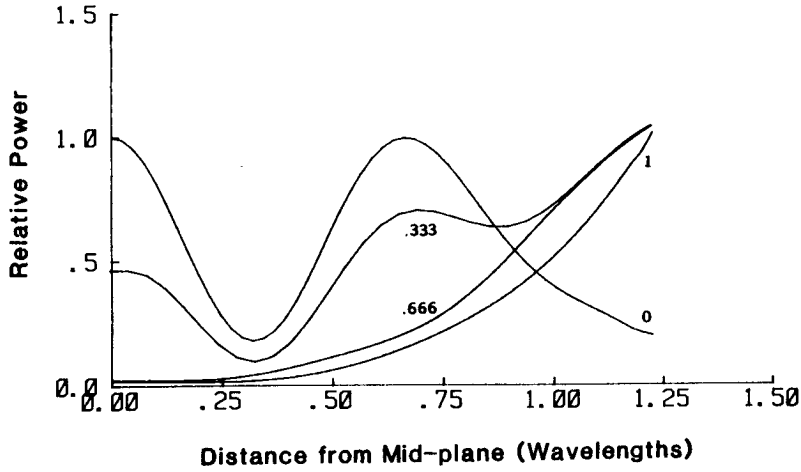

Figure 2.3.8 Power patterns for 915 MHz focussed planar source on axis and at .333, .666, and 1λ radius.

ted in Fig. 2.3.7. For the adjusted amplitude pattern, the focal point power and secondary maximum power levels are equal. These levels, in turn, are equal to the surface power for large ρ, as shown in Fig. 2.3.8, which repeats the amplitude adjusted pattern of Fig. 2.3.7 and shows the power pattern along parallel lines $(\rho, \theta) = (i0.333\lambda, 0), i = 1$, 2, 3. This figure also demonstrates that there are no other secondary maxima: the largest power levels are along the symmetry axis, $\rho = 0$.

Figure 2.3.8 represents the best possible power pattern for EM radiation at 915 MHz in an infinite slab of muscle tissue, in that a maximum amount of power is delivered to the deepest point without risking overheating any other regions. It is conceivable that a different choice of amplitude distribution might increase the ratio of focal point power to secondary maximum power without significantly suppressing the former below the surface power. However, this improvement would not exceed one or two percent, and since the measured values of the electrical parameters have a much wider variation, it is not useful to pursue further improvement.

The maximum thickness of 2.45λ corresponds to 11.1 cm at 915

MHz. This value compares well with the maximum diameter for any high resolution cylinder pattern, which is 12.6 cm from Table 2.1.1. Also, the focussed maximum thickness is more than three times the 3.6 cm maximum for the uniform source case of section 2.1.

Section 2.4 explores focussing the source for the cylindrical geometry where both modal analysis and an integral focussing are used.

2.4 Optimal Power Deposition in a Circular Cylinder

The cylinder is the last of the three simple geometries to be analyzed. There are many more applications for a cylindrical source since body parts, such as the limbs, neck, torso, and even the head can be modelled as cylinders. As expected, the penetration limits fall between those of the sphere and the planar slab.

It is interesting that the optimum cylindrical source synthesis case makes use of both of the design methods of the other two cases. As with the spherical analysis, the modal solutions to the wave equation restrict the distribution to a reduced set of functions. But instead of there being only one mode which contributes power at the focus, there is a family of cylindrical solutions which constructively add at the axis. These solutions are characterized by each being independent of circumferential variation. Although there are an infinite number of possible functions within this family, the synthesis problem is reduced from a two-dimensional one, as with the planar source, to a one-dimensional focussing design. The same phase/amplitude optimization method used with the plane can be applied to this reduced problem.

a. Optimal Source Derivation

The harmonic wave solutions for the cylindrical geometry are of the form [61]

$$E_{nm} = \hat{z} A_{nm} J_m(k_{\rho_n}\rho) e^{-jm\phi} e^{-jk_{z_n}z} \tag{1}$$

where J_m is the mth order cylindrical Bessel function, and with dispersion relation

$$k_{\rho_n}^2 + k_{z_n}^2 = \beta^2 - \alpha^2$$

The analysis problem involves summing a series of appropriately weighted functions of the form of (1) to give a maximum at $(\rho, z) =$

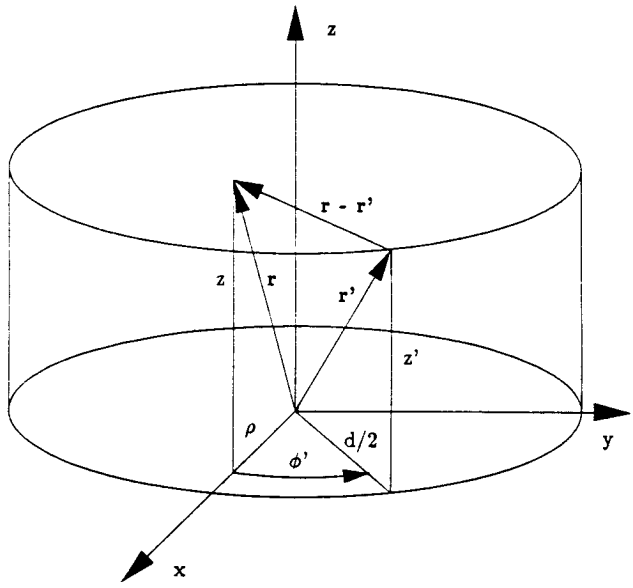

Figure 2.4.1 Coordinate geometry for cylindrical surface integration.

$(0,0)$. Recalling that $J_m(0)$ vanishes for all positive values of m, and $J_0(0) = 1$, it is clear that only harmonic solutions independent of the circumferential coordinate, ϕ, contribute to power on the axis. This is the restricted family of functions to be considered. For determination of the source distribution on a surface of constant radius, only the z-dependence remains to be determined.

To derive the optimum power pattern, the axial dependence of the best distribution is found by a focussed integral of the form of (1) in section 2.3. Analysis proceeds parallel to that of section 2.3. Figure 2.4.1 shows the geometry used for the integration over a cylindrical surface. An important difference between this geometry and the planar geometry is the choice of polarization. As discussed in section 2.1, the only acceptable source polarization is axial, or z-directed.

For a cylinder with radius $d/2$ and normal derivative taken with respect to $-\rho'$ so that waves propagate inwards to the focal target,

the operative formula for a cylinder is

$$\overline{E}(\overline{r}) = \int_0^{2\pi} \rho' d\phi' \int_{-\infty}^{\infty} dz' \left[\overline{E}(\overline{r}') \left(-\frac{\partial g(\overline{r}, \overline{r}')}{\partial \rho'} \right) - g(\overline{r}, \overline{r}') \left(-\frac{\partial \overline{E}(\overline{r}')}{\partial \rho'} \right) \right]_{\rho'=d/2} \tag{2}$$

with

$$|\overline{r} - \overline{r}'| = R = \sqrt{\rho^2 + \rho'^2 - 2\rho\rho' \cos\phi' + (z - z')^2} \Big|_{\rho'=d/2}$$

Note that the cylinder power pattern optimization is in terms of radius ρ, from the z-axis rather than distance z, from the mid-plane, as in the planar case. The source must, in this case be determined as a function of z'. Also, since there is only one cylindrical source surface rather than two opposing sources, only one integral needs to be computed.

Next, assume a source phase distribution similar to that in (3) of section 2.3 with surface phase $\Phi(z)$ to be determined, and an added power series in terms of ρ. This series is used to determine the normal field dependence $\partial\overline{E}/\partial\rho$. The series coefficients are once again found by using the eikonal equation (6) in section 2.3

$$\overline{E}(\overline{r}) = \hat{z} e^{j\Phi(z) - jk_\rho(\rho - \frac{d}{2}) - jk_{\rho 2}(\rho - \frac{d}{2})^2 - jk_{\rho 3}(\rho - \frac{d}{2})^3 - \cdots} \tag{3}$$

Equation (3) is evaluated on the integration surface, resulting in

$$\overline{E}(\overline{r}') \Big|_{\rho'=d/2} = \hat{z}\, e^{j\Phi(z')}$$

$$-\frac{\partial \overline{E}(\overline{r}')}{\partial \rho'} \Big|_{\rho'=d/2} = \hat{z}\,(jk_\rho) e^{j\Phi(z')} \tag{4}$$

with k_ρ to be determined in a similar manner as k_z in section 2.3.

The cylindrical wavefront normal is given by

$$\hat{n} = \frac{\hat{z}\frac{\partial \phi}{\partial z'} - \hat{\rho} k_\rho}{\sqrt{\left(\frac{\partial \Phi}{\partial z'}\right)^2 + k_\rho^2}} \tag{5}$$

and the eikonal equation (6) in section 2.3 results in

$$\begin{aligned} \Phi'^2 + \beta_\rho^2 - \alpha_\rho^2 &= \beta^2 - \alpha^2 \\ -2\alpha_\rho\beta_\rho &= -2\alpha\beta \end{aligned} \tag{6}$$

Note the similarity with (9) in section 2.3. The solutions for α_ρ and β_ρ are identical to those for α_z and β_z in (10) of section 2.3 with each z and ρ parameter interchanged.

Continuing the derivation, the normal derivative of the Green's function is

$$\begin{aligned} -\frac{\partial g(\bar{r},\bar{r}')}{\partial \rho'}\bigg|_{\rho'=d/2} &= (-jk - 1/R)\frac{e^{-jkR}}{4\pi R}\left(-\frac{\partial R}{\partial \rho'}\right)\bigg|_{\rho'=d/2} \\ &= (jk + 1/R)\frac{e^{-jkR}}{4\pi R}\left(\frac{d/2 - \rho\cos\phi'}{R}\right) \end{aligned} \tag{7}$$

Inserting (4) and (7) into (2) yields

$$\begin{aligned} \overline{E}(\bar{r}) = \frac{d/2}{4\pi}\int_0^{2\pi} d\phi' \int_{-\infty}^{\infty} dz' \Bigg[j\left(\frac{d/2 - \rho\cos\phi'}{R}\beta - \beta_\rho\right) \\ + \frac{d/2 - \rho\cos\phi'}{R}\left(\alpha + \frac{1}{R}\right) - \alpha_\rho \Bigg] \frac{e^{-j[kR - \Phi(z')]}}{R} \end{aligned} \tag{8}$$

At the focal point, $(\rho, z) = (0,0)$, $R_0 = \sqrt{z'^2 + (d/2)^2}$, and the maximum value of the integral of (8) occurs when the integrand is purely real and positive for all values of ϕ' and z'. The integrand is essentially the same form as in (12) of section 2.3, with z' replacing ρ', and dz' replacing $\rho' d\rho'$. The phase function, which makes the integrand positive at the focus, is thus identical in form to the phase functions derived in Table 2.3.1.

For $d/2 = 2\lambda$, at 915 MHz, the phase function correction due to complex amplitude and the series approximation error are plotted in Figs. 2.4.2 and 2.4.3. The phase function plot itself is so close to that presented in Fig. 2.3.3 for the function for $d/2 = 1.225\lambda$, that it is not repeated again here.

Determination of the maximum radius cylinder is considerably more straightforward than the similar problem for the plane. As with

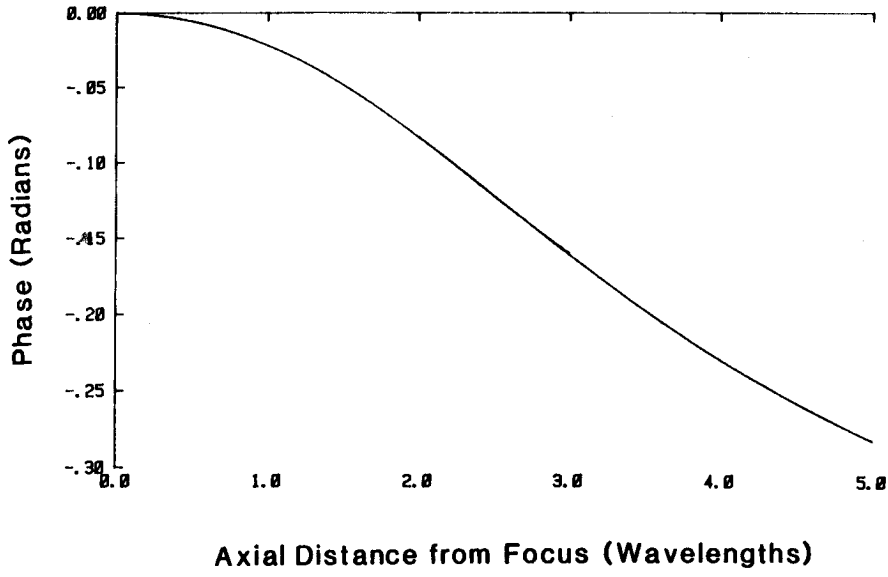

Figure 2.4.2 Correction function for complex integrand amplitude for focussing at 2.0λ depth.

the sphere, the secondary maxima are much lower than the focal point power maximum. This is the case even in the uniform pattern, Fig. 2.1.6. The limiting radius is once again arrived at iteratively, first by finding the focussed power at the focal point when focussed sources are at an arbitrary radius, say the uniform cylinder radius limit, $d/2 = 1.4\lambda$. This power value is 3.22. Extrapolating the uniform cylinder pattern out to the radius where the power level is 3.22 gives the first radius limit approximation. This radius value is used as the next $d/2$ parameter to recompute the focussed phase function. Then the unit amplitude, phase focussed source distribution is imposed at this radius, and the power at the focus is checked. Extrapolating the radius to the 3.22 power level turns out to be too large, since for larger radii cylinders, the focussing effects in lossy media are less pronounced. The $d/2$ radius is reduced in a third iteration step so that the power at a third $d/2$ radius is the same as at the axis. The iteration repeats until the desired accuracy is attained.

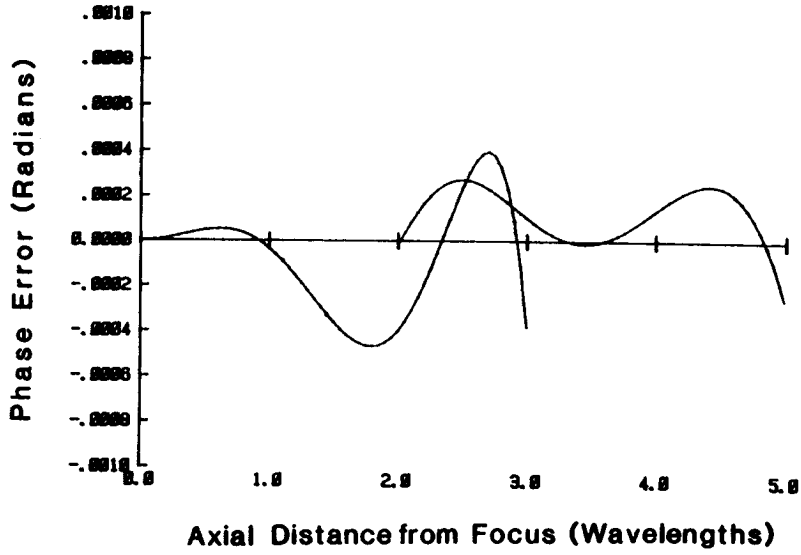

Figure 2.4.3 Approximation error for 2.0λ series.

The resulting focussed power pattern is depicted in Fig. 2.4.4, with the uniform pattern juxtaposed. These curves are computed by performing the integration in (8), which is most accurate near the focus, but begins to lose accuracy near the source surface. There are no direct ways to confirm the calculation of the focused pattern near the surface. The uniform pattern, however, can be represented in closed form (as in section 2.1, with a Bessel function) to compare to the integrated solution. As seen from Fig. 2.4.4, the agreement is excellent until about .3λ from the source.

The resolution near the axis is much greater and the power is 3.09 times higher than it is for a uniformly-exposed cylinder of the same radius; the largest allowable diameter is 36% larger, at 1.92 λ, or 17.3 cm at 915 MHz. This is large enough to be used in human limbs and neck, as well as in torsos of children. Compared to the sphere limits, it is seen that cylinder focussing approaches the fundamental limit of 18.9 cm. The maximum cylinder radius is only 3% less than the uniform current sphere radius, and 8.5% less than the best possible of all source configurations.

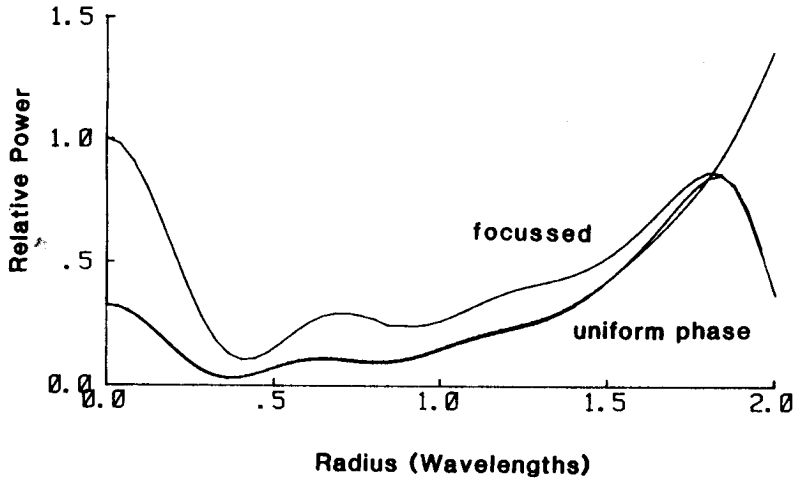

Figure 2.4.4 Optimized, focussed power pattern for a cylinder of muscle tissue at 915 MHz.

b. Summary and Results

The results of sections 2.2, 2.3, and 2.4 show that there is great potential for increasing the penetration limits of electromagnetic power, even in highly constrained geometries, over the currently accepted maxima. The results of the sphere analysis provide a fundamental limitation on the maximum depth for generating a local power peak. No other volume geometry will support as great a peak at the center. Although focussing produces much less concentration in lossy tissue than in free space, it still is prominent enough to significantly increase (up to a factor of 3 with a planar slab) the distance to the deepest point that can be safely heated.

The significant increase in maximum cylinder radius from 1.4 to 1.92λ at 915 MHz shows the effectiveness of axial focussing. This extension cannot be directly scaled to lower frequency, deeper penetrating waves. Although focussing always improves the pattern, higher α/β ratio keeps the electrical distance percentage increase smaller for lower frequencies. Figure 2.4.5 compares the focussed 100 MHz and 915 MHz patterns on a centimeter scale. The dashed lines indicate the extrapolations near the source where the integration approximations break

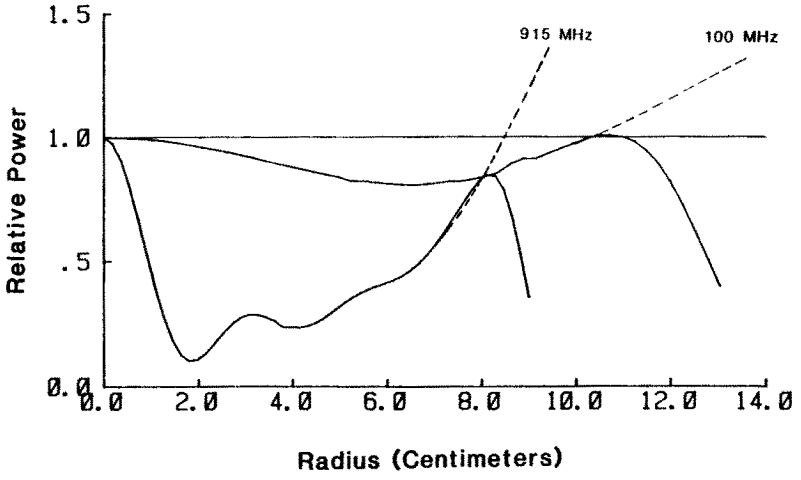

Figure 2.4.5 Comparison of radial power patterns for 915 MHz and 100 MHz focussed sources.

down. Focussing increases the 100 MHz maximum diameter from 19.0 cm (taken from Table 2.1.1) to about 21.0 cm, only a 10.5% increase. The lower frequency penetrates more deeply and would be preferable except for two difficulties. First, the power pattern resolution is not as sharp, with higher minima than with the 915 MHz pattern. Second and more importantly, few tumors are located in a cylindrical body part long enough to have the full aperture necessary for the full focussing effect. At 100 MHz, a 3-wavelength cylinder is 81 cm long.

The effects of truncating the infinite cylinder to represent a more practical antenna are examined in Fig. 2.4.6. Power dissipation curves as a function of radius are shown for 915 MHz, axially polarized, uniform surface power, 1.92λ radius sources with axial lengths 2λ, 4λ, 6λ, 10λ, and infinitely long. There is no perceptible difference between the 10λ and the infinitely long cylinder patterns. The truncation effects are significant for the narrow 2λ source, but the pattern rapidly converges to the ideal case for sources longer than the cylinder diameter.

At 915 MHz, the 17.3 cm maximum muscle diameter limitation allows high resolution heating for cancer cases in the head, neck and

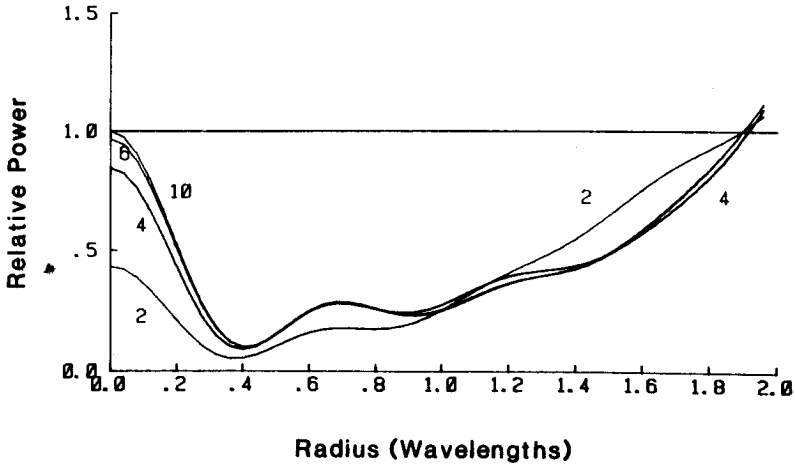

Figure 2.4.6 Power patterns for 915 MHz finite and infinite axial length focussed cylindrical sources.

limbs. Based on 1977 statistics [7], 11,600 brain; 9000 thyroid; 10,400 larynx; and 6,400 bone and soft tissue cancer cases per year may be suitable focussed cylindrical microwave source candidates. In each of these types of malignancy, the tumor is embedded in body structures which can readily be surrounded by electromagnetic sources, allowing a maximum geometric aperture advantage. Ultrasound, though much easier to focus in general, is impractical in these cases due to interference from bones. The last group of 6400 cases includes sarcomas that are prevalent in children, usually lead to limb amputation [3], would be a natural choice for EM applicators.

Electromagnetic hyperthermia offers a promising modality for treating cancer in humans. Important aspects including polarization, depth of heating, power profile resolution, secondary power maxima, and source distribution must be given careful consideration. Attempts have been made to synthesize power patterns and specify the maximum planar, cylindrical and spherical muscle dimensions for practical heating. Using a modal scheme for simplified geometries, followed by phase correction improvement — rather than experimental conjugate phase specification as suggested in the literature — leads to a pattern less likely to have undesirable hot-spots.

The recurrent theme with focussing in each geometry is the necessity of maintaining uniform surface power at the source *a priori.* The focussed source fields were derived starting by specifying uniform amplitude to ensure no isolated power maxima near the source. This is a novel concept, not previously discussed in the literature. The phase functions are solutions to the non-linear differential equation which makes the Kirchhoff integral formula purely real and positive. The optimum planar source has phase variation $\Phi(\rho)$ according to equations (15) and (16) in section 2.3. The optimal cylindrical source was shown to be polarized in the axial, z-direction, have no phase variation with ϕ and have a longitudinal phase variation function $\Phi(z)$ identical to the radial phase variation function $\Phi(\rho)$ as the planar case. Focussing tends to concentrate the interference effects on the axis (or plane) of phase symmetry for the planar (cylindrical) case which includes the focal point and intercepts the source.

The absolute power penetration limitations for muscle tissue have been determined and presented above. The fundamental limit for all geometries is a sphere of maximum radius as depicted in Fig. 2.2.5. For planar geometries, the best pattern has a slight amplitude reduction near the axis of symmetry which suppresses the secondary peak. The power pattern has equal power level at the focus, the distant source planes, and the secondary peaks. The maximum penetration depth is three times that of the uniform case. For cylindrical geometries, the source has uniform amplitude and a similar phase distribution to the planar case. The best focussed pattern has a maximum radius 35% larger than the uniform pattern radius.

The theoretical optimizations in this study are intended to serve as a set of idealized goals. Biological tissue is representative of dissipating media which is neither very conductive nor very insulating. Although few simplifying assumptions can be made for these intermediate cases, it is clear that focussing provides significant improvement over uniform illumination. This work is useful in many electromagnetic heating cases where the maximum surface power must be kept below a set limit, while deep power dissipation is maximized. Although many body structures may be modeled by the simple geometries considered above, the complete optimum antenna specification must also include tissue inhomogeneities, which in turn demands moment method analy-

sis. The focussing methods described herein are only a guide to be used for feasibility and initial applicator design. Hyperthermia cancer treatment is an exciting but challenging application of antenna synthesis, with much research still to be done.

Acknowledgments

I acknowledge the many helpful technical (and social) discussions with my advisor and mentor, Professor Frederic Morgenthaler. The advising help of the other members of my committee, Profs. Lele, Kong, and Kyhl is also appreciated.

This work was supported by NIH grant number CA 31303. This funding is gratefully acknowledged.

References

[1] Rappaport, C. M., *PhD Thesis*, Massachusetts Institute of Technology, 1987.

[2] Devita, V. T., S. Hellman, and S. A. Rosenberg, *Cancer, Principles and Practice of Oncology*, Lippincott, Philadelphia, 1982.

[3] Pace, O. T. and B. Cady, "Overal principles of cancer management, II. Surgery," in *Cancer: A Manual for Practitioners*, American Cancer Society, Boston, 1978.

[4] Holland, J. F. and E. Frei, *Cancer Medicine*, Lea and Rebiger, Philadelphia, 1982.

[5] Moosa, A. R., M. C. Robson, and S. C. Sahimoff, (ed.), *Comprehensive Textbook of Oncology*, Williams and Wilkins, Baltimore, 1986.

[6] Hahn, G. M., "Hyperthermia for the engineer: A short biological primer," *IEEE Biomedical Engineering*, **BME-31**, No. 1, 3–8, January 1984.

[7] Short, J. G. and P. F. Turner, "Physical hyperthermia and cancer therapy," *Proceedings of the IEEE,*, **68**, No. 1, 133–142, January 1984,

[8] Strohbehn, J. W. and E. B. Douple, "Hyperthermia and cancer therapy: A review of biomedical engineering contributions and challenges," *IEEE Trans. on Biomedical Engineering*, **BME-31**, No. 12, 779–787, December 1984.

[9] Westra, A. and U. C. Dewey, "Heat shock during the cell cycle of Chinese hamster cells *vitro*," *International J. of Radiation Biology*, **19**, 467–477, 1971.

[10] Palzer, R. J. and C. Heidelberger, "Studies on the hyperthermic killing on HeLa cells," *Cancer Research*, **33**, 415–421, 1973.

[11] Connor, W. G., E. W. Gerner, R. C. Miller, and M. L. M. Boone, "Prospects for hyperthermia in human cancer therapy, Part II," *Radiation Biology*, 197–503, May 1977.

[12] Storm, F. K., ed., *Hyperthermia in Cancer Therapy*, Prentice-Hall, Boston, MA, 1983.

[13] Hahn, G. M., *Hyperthermia and Cancer*, Plenum Press, New York, 1982.

[14] Song, C. W., "Effects of local hyperthermia on blood flow and microenvironment: a review," *Cancer Research*, **44**, 4721s–4730s, October 1984.

[15] Thrall, D. E., "Clinical requirements for localized hyperthermia in the patient," *Radiation and Environmental Biophysics*, **17**, 224–237, 1980.

[16] Meyer, J. L., "The clinical efficacy of localized hyperthermia," *Cancer Research*, **44**, 4745s–4751s, October 1984.

[17] Lai, P. K., C. A. Cain, and H. S. Ducoff, "Interaction between 2450 MHz microwaves and ionizing radiation in tribolium confusum," *IEEE Trans. Microwave Theory and Techniques*, **MTT-26**, No. 8, 530–534, August 1987.

[18] Crile, G., "The effects of heat and radiation on cancer implanted in the feet of mice," *Cancer Research*, **23**, 372–380, 1963.

[19] Dewey, W. C., "Interaction of heat with radiation and chemotherapy," *Cancer Research*, **44**, 4714s–4720s, October 1984.

[20] Lele, P. P. and J. K. Parker, "Temperature distributions in tissues during local hyperthermia by stationary or steered beams of unfocussed or focussed ultrasound," *British J. of Cancer*, **45-supplement V**, 108–121, 1982.

[21] Cheung, A. Y. and A. Neyzari, "Deep local hyperthermia for cancer therapy: External electromagnetic and ultrasound techniques," *Cancer Research*, **44**, 4736s–4744s, October 1984.

[22] Johnson, C. C. and A. W. Guy, "Nonionizing electromagnetic wave effects in biological materials and systems," *Proceedings of the IEEE*, **60**, No. 6, 692–718, June 1972.

[23] Guy, A. W., J. F. Lehmann, J. A. McDougall, and C. C. Sorenson, "Studies of therapeutic heating by electromagnetic energy," *Thermal Problems in Biotechnology*, 26–45, 1973.

[24] Guy, A. W., J. F. Lehmann, and J. B. Stonebridge, "Therapeutic applications of electromagnetic power," *Proceedings of the IEEE*, **62**, No. 1, 55–75, January 1974.

[25] Schwan, H. P. and K. R. Foster, "RF-field interactions with biological systems: Electrical properties and biophysical mechanisms," *Proceedings of the IEEE*, **68**, No. 1, 104–113, January 1980.

[26] Schwan, H. P., "Interaction of micrewave and radio frequency radiation with biological system," *IEEE Trans. on Micrewave Theory and Techniques*, **MTT-19**, No. 2, 146–152, February 1971.

[27] Stuchly, M. A. and S. S. Stuchly, "Dielectric properties of biological substances – tabulated," *J. of Microwave Power*, **15**, No. 1, 19–24, January 1980.

[28] Schwan, H. P., "Radiation biology, medical applications, and radiation hazards," in *Microwave Power Engineering*, E. C. Okress, ed., Academic Press, New York, **2**, 215–234, 1968.

[29] Guy, A. W., "Analyses of electromagnetic fields induced in biological tissyes by thermographic studies on equivalent phantom models," *IEEE Trans. on Microwave Theory and Techniques*, **MTT-19**, No. 2, 205–214, February 1971.

[30] Rappaport, C. M., "Localized hyperthermia with electromagnetic arrays and the leaky wave troughguide applicator," *IEEE Trans. on Microwave Theory and Techniqhes*, **MTT-34**, No. 5, May 1986.

[31] Storm, F. K., R. S. Elliot, W. H. Harrison, and D. L. Morton, "Clinical RF hyperthermia by magnetic loop induction: a new approach to human cancer therapy," *IEEE Trans. and Microwave Theory and Techniques,* **MTT-30**, No. 8, 1149–1157, August 1982.

[32] Ho, H. S., A. W. Guy, R. A. Sigelmann, and J. F. Lehmann, "Microwave heating of simulated human limbs by aperture sources," *IEEE Trans. on Microwave Thoery and Techniques,* **MTT-19**, No. 2, 224–231, February 1971.

[33] Morita, N. and J. B. Andersen, "Near-field absorbtion in a circular cylinder from electric and magnetic line sources," *Bioelectromagnetics*, **3**, No. 2, 253–274, 1982.

[34] Raskmark, P. and J. B. Andersen, "Focused electromagnetic heating of muscle tissue," *IEEE Trans. on Microwave Theory and Techniques*, **MTT–32**, No. 8, 887–888, August 1984.

[35] Andersen, J. B., "Focusing in lossy media," *Radio Science*, **19**, No. 5, 1195–1198, September 1984.

[36] Andersen, J. B., "Theoretical limitations on radiation into muscle tissue," *J. of Hyperthermia*, **1**, No. 1, April 1985.

[37] Gee, W., S. W. Lee, N. K. Bong, C. A. Cain, R. Mittra, and R. L. Magin, "Focused array hyperthermia applicator: theory and experiment," *IEEE Trans. on Biomedical Engineering,* **BME-31**, No. 1, 38–46, January 1984.

[38] Hand, J. W., J. L. Cheetham, and A. J. Hind, "Absorbed power distribution from coherent microwave arrays for localized hyperthermia," *IEEE Trans. on Microwave Theory and Techniques,* **MTT-34**, No. 5, 484–489, May 1986.

[39] Loane, J., H. Ling, B. F. Wang, and S. W. Lee, "Experimental investigation of a retro-focusing microwave hyperthermia applicator: conjugate-field matching scheme," *IEEE Trans. on Microwave Theory and Techniques,* **MTT-34**, No. 5, 490–494, May 1986.

[40] Hannemann, R. J. and J. E. Robinson, "Thermal analysis and design considerations for a dual-beam microwave applicator for hyperthermia research," *J. of Biomechanical Engineering,* **101**, 151–156, May 1979.

[41] Melek, M., B. Eng, and A. P. Anderson, "Theoretical studies of localised tumor heating using focused microwave arrays," *IEEE Proceedings,* **127F**, No. 4, 319–321, August 1980.

[42] Knoechel, R., "Capabilities of multiapplicator systems for focussed hyperthermia," *IEEE Trans. on Microwave Theory and Techniques,* **MTT-31**, No. 1, 70–73, January 1983.

[43] Massoudi, H., C. H. Durney, and C. C. Johnson, "A geometrical optic and an exact solution for internal fields in and energy absorption by a cylindrical model of a man irradiated by an electromagnetic plane wave," *Radio Science,* **14**, No. 65, 35–42, December 1976.

[44] Van Putten, M. H. P. M. and P. M. Van Den Berg, "A three-dimensional model for the 'coaxial TEM' deep body hyperthermia through layered tissue," *IEEE Trans. on Microwave Theory and Techniques,* **MTT-34**, No. 5, 526–531, May 1986.

[45] Sato, G., C. Shibata, S. Sekimukai, H. Wakabayoshi, K. Mitsuka, and K. Giga, "Phase controlled circular array heating equipment for deap-seated tumors: preliminary experiments," *IEEE Trans. on Microwave Theory and Techniques,* **MTT-34**, No. 5, 520–525, May 1986.

[46] Cudd, P. A., A. P. Anderson, M. S. Hawley, and J. Conway, "Phase array design considerations for deep hyperthermia through layered tissue," *IEEE Trans. on Microwave Theory and Techniques,* **MTT-34**, No. 5, 531–536, May 1986.

[47] Wait, J. R., "Analysis of the radiation leakage for a four aperture phased-array applicator in hyperthermia therapy," *IEEE Trans. on Microwave Theory and Techniques,* **MTT-34**, No. 5, 539–551, May 1986.

[48] Arcangeli, G., P. P. Lombardini, G. A. Lovisolo, G. Marsiglia, and M. Piattelli, "Focusing of 915 MHz electromagnetic power on

deep human tissues: a mathematical model study," *IEEE Trans. on Biomedical Engineering,* **BME-31**, No. 1, 47–52, January 1984.

[49] Morita, N., T. Hamasaki, and N. Kumagai, "An optical excitation method in multi-applicator systems forming a hot zone inside the human body," *IEEE Trans. on Microwave Theory and Techniques,* **MTT-34**, No. 5, 523–538, May 1986.

[50] Jouvie, F., J. C. Bolomey, and G. Gaboriand, "Discussion of capabilities of microwave phased arrays for hyperthermia treatment of neck tumors," *IEEE Trans. on Microwave Theory and Techniques,* **MTT-34**, No. 5, 495–501, May 1986.

[51] Turner, P. F., "Hyperthermia and inhomogeneous tissue effects using an annular phased array," *IEEE Trans. on Microwave Theory and Techniques*, **MTT-32**, No. 8, 874–882, August 1984.

[52] Turner, P. F., "Regional hyperthermia with an annular phased array," *IEEE Trans. Biomedical Engineering*, **BME-31**, No. 1, 106–114, January 1984.

[53] Gibbs, F. A., M. D. Sapozink, K. S. Gates, and J. R. Stewart, "Regional hyperthermia with an annular phased array in the experimental treatment of cancer: report of work in progress with a technical emphasis," *IEEE Trans. on Biomedical Engineering,* **BME-31**, No. 1, 115–119, January 1984.

[54] Hagmann, M. J., R. L. Levin, and P. F. Turner, "A comparison of the annular phased array to helical coil application for limb and torso hyperthermia," *IEEE Trans. on Biomedical Engineering,* **BME-32**, No. 11, 916–927, November 1985.

[55] Turner, P. F., "Mini-annular phased array for limb hyperthermia," *IEEE Trans. on Microwave Theory and Techniques*, **MTT-34**, No. 5, 508–513, May 1986.

[56] Sathiaseelam, V., M. F. Iskander, G. C. W. Howard, and N. M. Blechen, "Theoretical analysis and clinical demonstration of the effects of power pattern control using the annular phased array hyperthermia system," *IEEE Trans. on Microwave Theory and Techniques,* **MTT-34**, No. 5, 517–519, May 1986.

[57] Iskander, M. F., P. F. Turner, J. B. DuBow, and J. Kao, " Two-

dimensional technique to calculate the EM power deposition pattern in the human body," *J. of Microwave Power*, **17**, No. 3, 1982.

[58] Spiegel, R. J., "A review of numerical models for predicting the energy deposition and resultant thermal response of humans exposed to electromagnetic fields," *IEEE Trans. on Microwave Theory and Techniques*, **MTT-32**, No. 8, 730–746, August 1984.

[59] Weil, C. M., "Absorption characteristics of multilayered sphere models exposed to UHF/microwave radiation," *IEEE Trans. on Biomedical Engineering*, **BME-22**, No. 6, 468–476, November 1975.

[60] Kritikos, H. N. and H. P. Schwan, "The distribution of heating potential inside lossy spheres," *IEEE Trans. on Biomedical Engineering*, **BME-22**, No. 6, 457–463, November 1975.

[61] Kong, J. A., *Electromagnetic Wave Theory*, Wiley, New York, 1986.

[62] Hildebrand, F. B., *Advanced Calculus for Applications*, Prentice-Hall, Englewood Cliffs, NJ, 1976.

[63] Abramowitz, M. and I. A. Stegun, *Handbook of Mathematical Functions with Formulas, Graphs, and Mathematical Tables*, US Government Printing Office, Washington, DC, NBS Applied Mathematics Series – 55, 1972.

[64] Stratton, J. A., *Electromagnetic Theory*, McGraw-Hill, New York, 1941.

[65] Andersen, J. B., Private communication.

[66] Christensen, D. A. and C. H. Durney, "Hyperthermia production for cancer therapy: a review of fundamentals and methods," *J. of Microwave Power*, **16**, No. 2, 89–105, 1981.

[67] Tsai, C. T., C. H. Durney, and D. A. Christensen, "Calculated power absorption for hyperthermia applications consisting of electric dipole arrays," *J. of Microwave Power*, **19**, No. 1, 1–13, 1984.

[68] Wait, J. R., "Focussed heating in cylindrical targets: part 1," *IEEE Trans. on Microwave Theory and Techniques*, **MTT-33**, No. 7, 647–649. July 1985.

[69] Strohbehn, J. W. and R. B. Roemer, "A survey of computer simulations of hyperthermia treaments," *IEEE Trans. on Biomedical Engineering,* **68**, No. 1, 136–149, January 1984.

[70] Sultan, M. F. and R. Mittra, "An iterative moment method for analyzing the electromagnetic field distribution inside inhomogenous lossy dielectric objects," *IEEE Trans. on Microwave Theory and Techniques,* **MTT-33**, No. 2, 163–168, February 1985.

[71] Holt, F. S., "Application of geometric optics to the design analysis of microwave antennas," *Tech. report AFCRL-67-0501*, Air Force Cambridge Research Laboratory, September 1967.